KYOTO UNIVERSITY

Study of Neutrinos from Monopole-Catalyzed Proton Decay in Super-Kamiokande

DISSERTATION

submitted in partial satisfaction of the requirements
for the degree of

MASTER

in Physics

by

Feng Jiahui

2021

DEDICATION

To Feng Family

TABLE OF CONTENTS

LIST OF FIGURES

LIST OF TABLES

ACKNOWLEDGMENTS

First of all, I need to thank my advisor teacher Roger Wendell. Thanks to him, this paper was completed. During my research, he gave me a lot of useful suggestions, and he was able to find errors that I could not find very sensitively at the same time. At the same time, thanks to his advice, I gradually improved my programming level and laid a solid foundation for my future Ph.D. study. At the same time, thanks to his daily chats, I have a deeper understanding of American culture. It can be regarded as the greatest consolation in 2020 when the COVID-19 virus epidemic.

Secondly, I also need to thank Professor, Nakaya Tsuyoshi, who allowed me to come to Japan and allowed me to participate in the world-class Super Kamiokande experiment. At the same time, he also gave me a lot of help in life when I first came to Japan.

After that, I would like to thank Ashida Yosuke, my Japanese teacher in some sense. He gave me a lot of help when I first came to Japan and needed to adapt to the new school and new environment. His hearty character and very personal Japanese characteristics left me with very fond memories.

And Tani Mao. Everything in my life in Japan could not go on normally without him. He helped me a lot, especially at the hardest moment in my life. I hope he can live well for the rest of his life.

Then I would like to thank Mori Masamitsu, who played a very important role in my final research phase. At the same time, thanks to him, I was able to make great progress in hardware work.

At the same time, I would also like to thank the members of the Super Kamioka Experimental Cooperation Group, especially these people, Makoto Miura, Shunichi Mine, Takuya Tashiro, Yasuhiro Nishimura, Christophe Bronner, whose suggestions have played a very important role in my research.

I also need to thank the administrative staff of Kamioka, who carefully guided my life and accommodation in Kamioka.

Finally, I would like to thank my classmates at Kyoto University, Kobayashi Ren, Sueno Yoshinori, Tsujikawa Yoshiaki, Sugashima Bungo. Although our research directions are not together, it is really because of them that I have had a wonderful two and a half years.

ABSTRACT OF THE DISSERTATION

Study of Neutrinos from Monopole-Catalyzed Proton Decay in Super-Kamiokande

By

Feng Jiahui

Master in Physics

Kyoto University , 2021

The symmetry of the electromagnetic field is the diamond of the physics crown. Maxwell describes the electromagnetic field by ultimately beautiful mathematics. However, there is a cloud just hanging on the top of this diamond. We have already found the single charged particles such as electron and position, electric charge, but we still haven't found the existence of a magnetic monopole.

The Grand Unified Theory (GUT), which was born when people were looking for the ultimate symmetry, predicts the existence of magnetic monopoles. The Rybakov effect also predicts that magnetic monopoles will catalyze the proton decay, the most important prediction of the GUT. Therefore, this effect will become a powerful tool to search for magnetic monopoles and verify the grand unified theory. Magnetic monopoles created in the early universe could be captured in the sun, where they catalyzes the decay of its hydrogen. The decay is mainly divided into direct decay and indirect decay. Both of these decay modes could produce neutrinos with different energies.

The Super-Kamiokande experiment is a water Cherenkov experiment and is mainly used to explore various neutrino physics. The SK collaboration has completed the analysis for searching the indirect proton decay mode. The result is the flux of monopoles in the universe $F_{\mathrm{M}}\left(\frac{\sigma_0}{1\mathrm{mb}}\right)\left(\frac{f_{\pi^+}}{0.5}\right) < 6.3\times10^{-24}\left(\frac{\beta_{\mathrm{M}}}{10^{-3}}\right)^2$ cm^{-2} s^{-1}sr^{-1}(90% C.L.). However, there also have great potential for exploring magnetic monopoles through direct proton decay. In this the-

sis we perform a sensitivity analysis of the neutrinos, produced when magnetic monopoles catalyze direct proton decay, based on Super-Kamiokande experiment. The result of the Asimov sensitivity analysis is $F_M \left(\frac{\sigma_0}{1\text{mb}}\right) \left(\frac{BR_{p\to\bar{\nu}}}{10^{-4}}\right) < 4.01 \times 10^{-26}$ cm^{-2} s^{-1}sr^{-1}(90% C.L.). This result is two orders of magnitude smaller than the indirect proton decay mode, so it indicates that the search for such neutrinos from the catalyzed direct decay can provide strong constraints on magnetic monopoles.

Chapter 1

Introduction

1.1 The magnetic monopole

The symmetry of the electromagnetic field is the diamond of the physics crown. Maxwell describes the electromagnetic field by ultimately beautiful mathematics. However, there is a cloud just hanging on the top of this diamond. We have already found the single charged particles such as electron and position, electric charge. That leads to the next question, does the universe have single magnetic charges, so-called magnetic monopoles?

In 1885, Heaviside changed the Maxwell equation, assuming monopoles exist, inducing a symmetry withe the electron equations:

$$\nabla \cdot \mathbf{D} = \rho_e, \quad \nabla \times \mathbf{E} + \dot{\mathbf{B}} = -\mathbf{J}_m, \quad \nabla \cdot \mathbf{B} = \rho_m, \quad \nabla \times \mathbf{H} - \dot{\mathbf{D}} = \mathbf{J}_e. \tag{1.1}$$

We can see that this equation has a beautiful symmetry, the monopole electron symmetry. In the equation $\mathbf{J}_e$ is the current density, ρ_m is the magnet density, and $\mathbf{J}_m$ is the magnetic field density. The magnetic charge is conserved as is the electric charge.

1.1.1 The Dirac monopole

In 1931, Dirac found out that if we want to explain how the electric charge is quantized [19], there should be in the universe, if there is only one. More precisely, we can use the following equation to describe the relationship of the monopole and how the electric charge is quantized:

$$\frac{eg}{\hbar} = 2\pi n. \tag{1.2}$$

In this equation e is the elementary charge, g is the monopole's magnetic charge, and n is an integer which should be 0, ±1, ±2.

We can't estimate the mass of the monopole with this equation. However, if we assume the radius of the monopole is same as that of the electron, we can estimate the mass of Dirac monopole is $r_M = \frac{g^2}{m_M c^2} = r_e = \frac{e^2}{m_e c^2}$, and $m_M = \frac{g^2 m_e}{e^2} \simeq n4700 m_e \simeq n2.4\text{GeV}/c^2$.

After Dirac predicted the monopole has exists, scientists have been trying to search the monopole with accelerators. The most recent effort was published in 2006, Fermi Lab. Scientists try to search monopole by using electron-positron collisions at $\sqrt{s} = 1.96\text{TeV}, 35.7\text{pb}^{-1}$. The is result shows no any signature of a light monopole (mass of monopole is lighter than $360\text{GeV}/c^2$) [5].

1.1.2 Grand Unified Theory monopole

In 1974, Hooft and Polyakov found that maybe some perturbation solution of the quantum field theory could describe the magnetic monopole [34, 20]. This prediction shows that the monopole is a necessary part of the universe, the same as Dirac prediction.

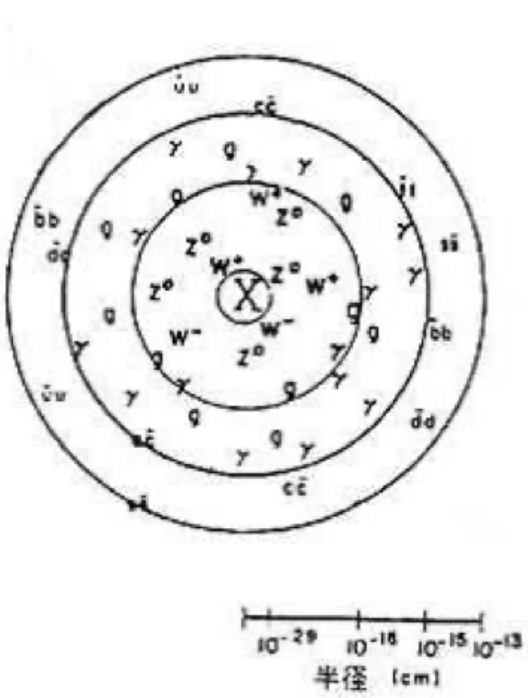

Figure 1.1: One possible structure of a Grand Unified Theory monopole. [10]

GUTs Magnetic monopoles have an onion-like structure that contains all the interactions of the Grand Unified Theory. Figure 1.1 shows a possible structures of the Grand Unified Theory magnetic monopole.

In the core (radius 10^{-29} cm), the symmetry of the Grand Unified Theory is restored, and X and Y bosons can be exchanged. There is an electroweak area (10^{-16} cm) on the outside, where W, Z0 bosons interact. Furthermore, the outside (10^{-13}cm) is a confinement area, which is composed of photons and gluons. Outside this electroweak area, is the fermion-anti-fermion condensation region. If we observe the GUTs monopole from afar, it will behave as a point particle like a Dirac magnetic monopole that produces a magnetic field [10].

GUTs predict that monopoles will be produced in the phase transition in the early universe. If we assume the GUT has the gauge group SU(5), the phase transition and the

transition temperature will like below:

$$\mathrm{SU(5)}\frac{10^{15}\mathrm{GeV}}{10^{-35}\ \mathrm{s}}\mathrm{SU(3)_C}\times[\mathrm{SU(2)_L}\times\mathrm{U(1)_Y}]\,\frac{10^{2}\mathrm{GeV}}{10^{-9}\ \mathrm{s}}\mathrm{SU(3)_C}\times\mathrm{U(1)_{EM}}. \tag{1.3}$$

Here, the numerator represents the transition temperature of each phase transition, and the denominator represents the time with each phase transition occurs when the beginning of the universe is taken as the time origin.

At the SU(5) phase transitions monopoles will be produced on the horizon. We can estimate the monopole density is $\rho_M \sim 5\times10^{-18}$ g/cm^3 under the hypothesis of steady state cosmology. However, this number far exceeds the observation $\rho_c < 10^{-29}$ g/cm^3 [55]. This problem is called the monopole excess problem.

In 1981, the inflation universe theory [28, 61] make significant progress in solving the steady-state cosmology problems, like the monopole excess problem. Universe inflation, or inflation for short, is a process in which space expands rapidly during the early universe. The period of inflation started 10^{-36} seconds after the Big Bang and lasted between 10^{-33} and 10^{-32} seconds. After inflation, the universe continues to expand but at a much slower speed. At this time, the inflation field decays into different particles.

1.1.3 The Rybakov effect

GUTs predict the proton will interact with the GUT bosons X, Y in some situations, and then this proton will decay into a lepton and some meson with some monopole as the catalyst. However, this reaction has a small cross-section is about $\sigma \sim 10^{-56}$cm^2. That means this reaction will not happen in normal energy scales.

Nevertheless, in 1983, Rybakov and Callan found that catalyzation the mass of monopole will not suppress cross-section. The Rybakov effect is a phenomenon in which the s wave

component of fermions is rapidly increases near the core of the magnetic monopole. In other words, while the wave function with finite angular momentum is strongly suppressed near the core, only the s wave component can effectively interact with the core. This means the cross-section has a constant value, about $\sigma_0 \sim 1$ Mb.[60, 69]. That shows that the monopole catalyzed proton decay will have the same strengths as the normal strong interaction. This result is called the Rybakov effect.

$$M + p \to M + e^+ + \pi^0. \tag{1.4}$$

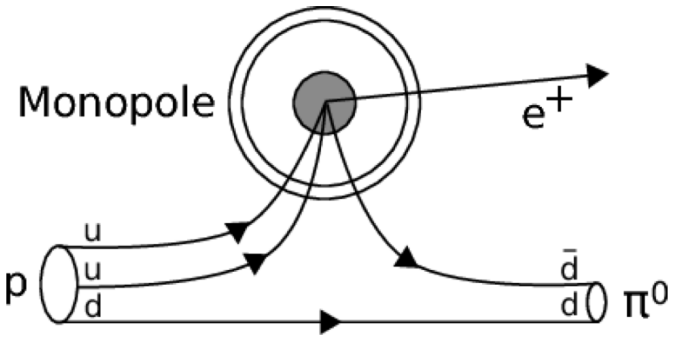

Figure 1.2: Heuristic diagram of monopole-induced proton decay. [1]

1.2 Review of Magnetic monopole searches

The GUTs monopole is very heavy compared with another particle which have already been found. However, we can search for the monopoles that were generated in the early universe. So far there is no experimental evidence for monopoles. [24].In the following we show some of the limits from experiments and theoretical predictions..

1.2.1 Monopole flux limit from the electromagnetic induction experiment

If we assume the monopole is flying all over the universe, then when the magnetic monopole passes through a coil, it will induce in the ring an electromotive force and a permanent current (Δi). For a coil with N turns and inductance L, $\Delta i = 4\pi N n g_D/L = 2\Delta i_o$, where Δi_o is the current change corresponding to a change of one unit of the flux quantum of superconductivity and ng_D is the total magnetic charge of the GUTs monopole, which go through coils [15, 23].

This search method has a great advantage for detecting monopole. Because this method does not rely on the speed of the monopole, so we can measure the monopole flux in a huge speed range. However, this measurement requires an exact sensitivity to the monopole signal, so we have to use the superconductive coil. Because of the financial problem, it will not be easy to build a superconductive coil that could cover a huge area. Moreover, it is also difficult to reduce the background noise of the superconductive coil since the monopole signal is quite small. The limit which comes from the superconductive coil result is [25]

$$F < 2 \times 10^{-14}\ \mathrm{cm}^{-2}\ \mathrm{s}^{-1}\mathrm{sr}^{-1}. \tag{1.5}$$

1.2.2 Monopole flux limit from the electromagnetic energy losses experiment

There are several ways to measure the monopole flux by using the electromagnetic energy losses. Such as, we could use the plastic track detector, the scintillation counter, or proportional counter.

When a magnetic monopole passes through plastic, polymerization and radiation dam-

age occurs along the track. Therefore, a limit can be set by searching for the track of the magnetic monopole by chemical treatment. While plastic is inexpensive, making a large area detector is easy, and the limit can be tightened.

The scintillation counter is a method, which searches for scintillation light emitted by atoms and molecules that are excited and return to the ground state when magnetic monopoles pass through a liquid or gas. Another method is proportional counter, which is used the signal generated by the ionized gas electrons when the magnetic monopole goes through the proportional counter. All of the experimental method have have been used to search for the monopole. Experimental results are listed in table 1.1.

Table 1.1: Summary of the monopole flux limit come from the electromagnetic energy losses experiment.

Experimental type	β range	Limit
plastic track detector	$10^{-2} < \beta < 1$	$F < 3.2 \times 10^{-16}$ cm^{-2} s^{-1}sr^{-1} [52]
scintillation counter		$F < 6.6 \times 10^{-14}$ cm^{-2} s^{-1}sr^{-1} [27]
proportional counter		$F < 8.7 \times 10^{-15}$ cm^{-2} s^{-1}sr^{-1} [24]

1.2.3 Monopole flux limits from theory

Limit from the universe density .

This limit assumes that the mass density of the universe is less than the critical density, which is calculated assuming the universe is flat (cosmological constant $\Lambda = 0$) . If we take the mass of the monopole as m_M, and the speed of the monopole is β, the limit value is

$$F = \frac{n_M \beta c}{4\pi} < 3 \times 10^{-14} h^2 \left(\frac{\beta}{10^{-3}}\right) \left(\frac{10^{16}\text{GeV}}{m_M}\right) \text{cm}^{-2}\ \text{s}^{-1}.\text{sr}^{-1} \tag{1.6}$$

Here h is the Hubble parameter, $h \equiv H_0/100\text{kms}^{-1}\text{Mpc}^{-1}$, and $H_0 \sim 70\text{kms}^{-1}\text{Mpc}^{-1}$, and it assume the monopole is uniformly distributed in the universe.

Limit from the magnetic field .

Because the galaxy is not uniformly distributed, a magnetic field is generated from the flow of cosmic rays since it contains the amount of the charged particles. The magnetic field strength is about 3μG. Monopoles will be accelerated by the magnetic field. If the monopole go through the galaxy, then the monopole will get the energy from galaxy like

$$E_{-} = \pi r_G^2 \sqrt{\frac{r_G}{\ell}} (gB\ell) 4\pi F \tau_G. \tag{1.7}$$

Here, r_G is the radius of the galaxy, ℓ is the galactic magnetic field range, and the g is the magnet charge of the monopole. B is the galaxy magnetic field strength. If the magnetic field accelerates the monopole there will by a dynamo with energy generated like

$$E_{+} = \frac{B^2}{2} \frac{4\pi r_G^3}{3}. \tag{1.8}$$

If the monopole generates, the energy is more significant than the energy of monopole lost in the galaxy, then the galactic magnetic field will be annihilated. However, we find the galaxy magnetic field has not been annihilated in this way. [13]. We can therefore restrict the monopole flux by this assumption. This monopole flux limit is called Parker limit [27].

$$F < 10^{-15} \left(\frac{B}{3\mu\text{G}}\right) \left(\frac{r_G}{30\text{kpc}}\right)^{1/2} \left(\frac{300\text{pc}}{\ell}\right)^{1/2} \left(\frac{30\text{Myr}}{\tau_G}\right) \text{cm}^{-2}\ \text{s}^{-1}\text{sr}^{-1}. \tag{1.9}$$

1.2.4 Limit from the previous search in Super-Kamiokande

This thesis searches for monopoles trapped within the Sun. Firstly, we assume that a monopoles present in the universe. Second, if those monopels are gravitationally captured by the sun, they have a high probability to catalyze proton decay herein. So we search for neutrinos from proton decays in the Sun as our signal.

The Rybakov effect predicts that the monopole is cannot easily catalyze odd nuclei since the odd nuclei, with odd atomic number are bosons. However, the Rybakov effect only happened in fermion. Therefore, the odd nuclei have a great repulsion with the monopole. Consequently, we cannot look forward to giving a solid limit by searching for monopole-catalysis-proton-decay neutrino in odd nuclei-dominated planets, such as Earth or Mars. However, focusing on Sun or Jupiter, they are full of the free proton. Therefore, we might search monopole flux by measuring the monopole-catalysis-proton-decay neutrino from these objects.

There are two types of decay mode in monopole catalyzed proton decay, the indirect decay mode, and the direct decay mode.

The first one is the proton decay into meson and charged lepton.

$$p \to \left(\rho^0, \omega, \eta, K^+, \cdots\right) + e^+ \left(\text{or } \mu^+\right). \tag{1.10}$$

The heavy meson will decay into π^+ and π^- . Because the negative charged particle will be absorbed in the sun, we don't consider them

$$\left(\rho^0, \omega, \eta, K^+, \cdots\right) \to \pi^+ \tag{1.11}$$

$$\pi^+ \to \mu^+ \nu_\mu \tag{1.12}$$

$$\mu^+ \to e^+ + \nu_e + \bar{\nu}_\mu. \tag{1.13}$$

If we only consider the π^+ particles which are generated by the proton decay meson decay, it will finally decay into charged lepton and neutrino. Also, one of the charged lepton, muon, could decay into neutrino too. Consequently, this type of decay mode will generate several neutrinos, which will arrive on Earth and be detected by the Super-Kamiokande ex-

periment. Because they are generated from the decay of meson or charged lepton, therefore, the energy of these neutrinos is restricted by the mass of the mesons and the charged lepton. The result shows that the momentum of the monopole-catalyzed-proton-decay neutrino in this proton decay mode is only between 20 to 50 MeV.

This two-step-proton-decay mode neutrino has already been studied in Super-Kamiokande in 2012 [68]. The monopole flux limit given by this search is shown in Figure 1.3.

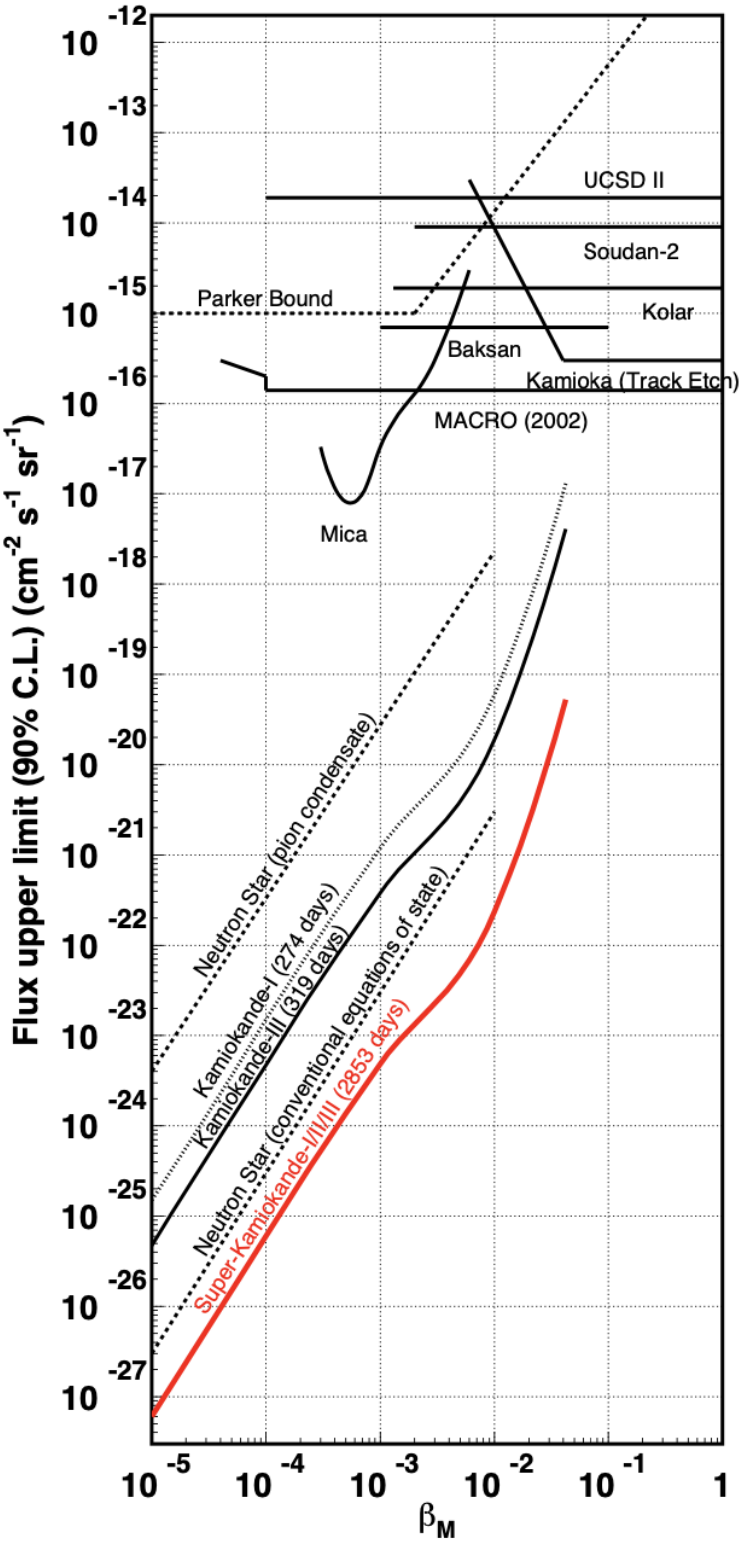

Figure 1.3: The upper limits on the monopole flux as a function of monopole velocity, red line is the previous monopole analysis in Super-Kamiokande by using indirect proton decay at 90%C.L , β_M. Catalysis cross section (σ_0=1mb) and monopole mass ($M_M = 10^{16}$ GeV) are assumed for indirect searches.[68]

However, from the recent theoretic result, we find the previously forbidden monopole catalyze proton decay channel, the 'direct' decay mode, [35]

$$p \to \bar{\nu_e} + \pi^+ \tag{1.14}$$

It becomes another possible channel to discover the monopoles. Previously, this decay mode was considered was forbidden because monopole only carries $\mathrm{SU(3)_C \times U(1)}$. However, the $\mathrm{SU(3)_C \times U(1)}$ will be resolved to the Standard Model group, $\mathrm{SU(3)_C \times SU(2)_L \times U(1)}$. If we consider this limit, the restriction will not be valid anymore. Furthermore, the two-step proton decay mode will be suppressed by the electroweak suppression factor. Indeed, the direct proton decay mode will have better discovery potential than the two-stage proton decay mode.

The direct proton decay, flux is estimated as follows:

$$F_{\bar{\nu}} \sim 1.4 \times 10^4 \left(\frac{\sigma_0}{0.1\mathrm{mb}}\right) \left(\frac{\beta}{10^{-3}}\right) \left(\frac{BR_{p\to\bar{\nu}}}{10^{-4}}\right) \left(\frac{N_M}{10^{25}}\right) \mathrm{cm}^{-2}\ \mathrm{s}^{-1}\mathrm{sr}^{-1}. \tag{1.15}$$

where the σ_0 is Rybakov effect cross-section , β is the velocity of the monopole, and $BR_{p\to\bar{\nu}}$ is corresponding branching ratio. The characteristic neutrino energy is

$$E_{\bar{\nu}} = \left(m_p^2 - m_{\pi^+}^2\right)/2m_p = 458.755\mathrm{MeV}. \tag{1.16}$$

Although the emitted neutrinos are a single flavor in the Sun, this neutrino will oscillate into different neutrino flavors when they arrive on Earth. Furthermore, the different neutrino flavors will interact with SK in different ways. Therefore, we must consider the neutrino

oscillation weight as follows.

$$\begin{aligned} P\left(\nu_\alpha \to \nu_\alpha\right) =& 1 - 4\left|U_{\alpha 2}\right|^2\left(1-\left|U_{\alpha 2}\right|^2\right)\sin^2\frac{\Delta_{21}}{2} - 4\left|U_{\alpha 3}\right|^2\left(1-\left|U_{\alpha 3}\right|^2\right)\sin^2\frac{\Delta_{31}}{2} \\ &+ 2\left|U_{\alpha 2}\right|^2\left|U_{\alpha 3}\right|^2\left(4\sin^2\frac{\Delta_{21}}{2}\sin^2\frac{\Delta_{31}}{2} + \sin\Delta_{21}\sin\Delta_{31}\right) \end{aligned} \tag{1.17}$$

$$\begin{aligned} P\left(\nu_\alpha \to \nu_\beta\right) =& 4\left|U_{\alpha 2}\right|^2\left|U_{\beta 2}\right|^2\sin^2\frac{\Delta_{21}}{2} + 4\left|U_{\alpha 3}\right|^2\left|U_{\beta 3}\right|^2\sin^2\frac{\Delta_{31}}{2} \\ &+ 2\Re\left(U^*_{\alpha 3}U_{\beta 3}U_{\alpha 2}U^*_{\beta 2}\right)\left(4\sin^2\frac{\Delta_{21}}{2}\sin^2\frac{\Delta_{31}}{2} + \sin\Delta_{21}\sin\Delta_{31}\right) \\ &+ 4J_{(\alpha,\beta)}\left(\sigma^2\frac{\Delta_{21}}{2}\sin\Delta_{31} - \sin^2\frac{\Delta_{31}}{2}\sin\Delta_{21}\right). \end{aligned} \tag{1.18}$$

We use the same notation as shown in [6], where $\Delta_{ij} \equiv \delta m^2_{ij} L/2E = 2.534\left(\frac{\delta m^2_{ij}}{\mathrm{eV}^2}\right)\left(\frac{\mathrm{GeV}}{E}\right)\left(\frac{L}{\mathrm{km}}\right)$, the Jarlskog invariant is taken as, $J_{(\alpha,\beta)} = \Im\left(U^*_{\alpha 1}U_{\beta 1}U_{\alpha 2}U^*_{\beta 2}\right)$. If we assume the Sun-Earth distance is 1.496×10^8 km, then the oscillation probability for $\bar{\nu_e}$ and $\bar{\nu_\mu}$ are.

$$P\left(\bar{\nu}_e \to \bar{\nu}_e\right) \approx 0.38 \tag{1.19}$$

$$P\left(\bar{\nu}_\mu \to \bar{\nu}_e\right) \approx 0.47 \tag{1.20}$$

and the monopole catalyze proton decay neutrino fluxes are.

$$F_{\bar{\nu}_e} \approx 5.3 \times 10^3\left(\frac{\sigma_0}{0.1\mathrm{mb}}\right)\left(\frac{\beta}{10^{-3}}\right)\left(\frac{BR_{p\to\bar{\nu}}}{10^{-4}}\right)\left(\frac{N_M}{10^{25}}\right)\mathrm{cm}^{-2}\ \mathrm{s}^{-1}\mathrm{sr}^{-1} \tag{1.21}$$

$$F_{\bar{\nu}_\mu} \approx 6.6 \times 10^3\left(\frac{\sigma_0}{0.1\mathrm{mb}}\right)\left(\frac{\beta}{10^{-3}}\right)\left(\frac{BR_{p\to\bar{\nu}}}{10^{-4}}\right)\left(\frac{N_M}{10^{25}}\right)\mathrm{cm}^{-2}\ \mathrm{s}^{-1}\mathrm{sr}^{-1}. \tag{1.22}$$

This thesis search antineutrino generated by the direct proton decay mode in the Super-Kamiokande experiment. This neutrino flux is a mono-energetic 459 MeV antineutrino flux that comes from the Sun.

In chapter 2, We will introduce the Super-Kamiokande experiment. In chapter 3, We will introduce the event reconstruction. In chapter 4, We will introduce the event simulation. In chapter 5, We will talk about the event selection, and in the final chapter, the sensitivity estimation using the SK4 Monte Carlo (MC) will be introduced.

Chapter 2

Super-Kamiokande Experiment

2.1 Detector Description

Super-Kamiokande (SK) is a detector that consists of 13000 photomultipliers (PMT) and a cylindrical stainless steel water tank full of 50,000 tons ultra pure water. The water tank is 39.3 m in diameter and 41.4 m high. This tank is buried under 1000 m of the Mountain Ikenoyama, in Kamioka town, Hida City, Gifu Prefecture, Japan. This buried is mainly to reduces the cosmic ray background, the main background of SK. Because SK is a water Cherenkov light detector, it detects the Cherenkov light generated by the charged particles when that particle goes through the water. The buried depth the cosmic muon flux is $6 \times 10^{-8}\mathrm{cm}^{-2}\mathrm{s}^{-1}\mathrm{sr}^{-1}$ which is about 1×10^{-5} magnitude compared with earth surface flux.

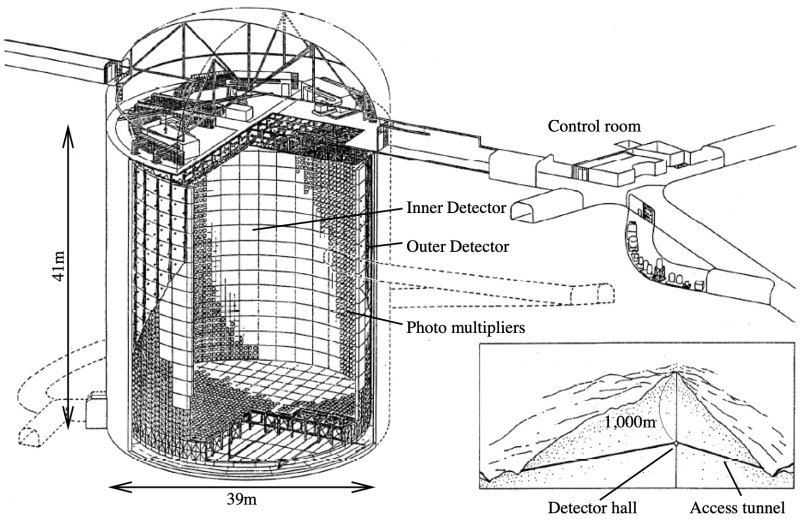

Figure 2.1: Overview of the Super-Kamiokande detector.[38]

2.1.1 The structure of the Super-Kamiokande Experiment

SK is a detector separated into two parts. The inner detector is called ID, and outer part is called OD. Furthermore, there has a 55 cm wide steel-support structure to support PMTs.

The ID is positioned 2.6m from the wall of the SK and contains about 32 kilotons of water and uses about 11,000 20-inch PMTs which are facing inward. The space between the ID PMTs is covered with a black sheet to reduce the unexpected photon reflection. The ID PMT is installed in modules. Each of the modules holds 3×4 PMTs.

The OD is placed 2.2m from the wall of the SK tank and 2.1m from the top and bottom of the tank. It contains 18 kilotons of water. The main target for the OD is to reject the cosmic ray particles and the particles emitted by the rock of the mountain. It is uses 1885 8-inch PMTs. These PMTs face outward from the support structure. The Tyvek sheet covers the space between the OD PMTs to maximize the light detection efficiency.

Apart from this equipment, there are also 26 Helmholtz coils to avoid the earth's mag-

netic field from disturbing the PMTs. The surface of SK has five electronic huts and a linear accelerator for detector calibration.

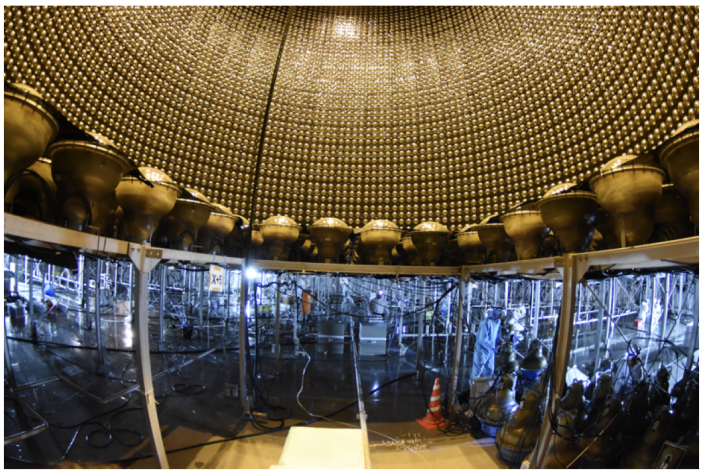

Figure 2.2: Photo from the bottom of the tank renovation in 2018. The upper part in the center of the photo is the inner water tank, and the lower part is the outer water tank.[67]

Figure 2.3: A photo looking up from the bottom of the OD. An 8-inch PMT is attached to the wall on the inner tank side, and the outer tank is covered with a white Tyvek sheet.[67]

2.1.2 History of the Super-Kamiokande Experiment

The SK start construction in 1991 as a successor to the Kamioka-NDe experiment. The mining company excavated the cavity of the mine in 1994. Afterward, the PMT install work finished in 1995. After a one-month test operation, SK officially started on 1996 1 April. The SK data-taking period is divided into six parts as of 2020.

The first period is called SK1. It starts on 1 April 1996, ends in July 2001. In the SK1 period, there are 11146 PMTs is installed in the ID, and the photo coverage is about 40%.

On 12 November 2001, one of the bottom PMTs imploded during a post-maintenance tank refill. This accident caused 7796 PMTs to be damaged (66779 ID PMTs and 1017 OD PMTs). The other PMTs which could still work rearranged to were resume observation. Furthermore, every PMTs has since been covered with acrylic and fiberglass reinforced plastic (FRP) to protect the PMT so as not cause a subsequent chain reaction. This observation period starts from October 2002 to October 2005, is called SK2. There are 5182 ID PMTs and 1885 OD PMTs, and the photo coverage of ID is 19%.

In October 2005, newly produced PMTs were installed to the tank. This work is finished in 2006 July, and the entire operation 11129 ID PMTs was resumed. The photo coverage is still 40%. This data period from July 2006 to August 2008 is called SK3.

The SK4 is the most prolonged data-taking period, lasting from September 2008 to June 2018. The most different point compared with SK3 is that SK upgraded all of the front-end electronics.

In June 2018, other upgrades and repairs were started. The goals were repairing the leak of the SK tank, installing a new plumbing system, and replacing dead ID and OD PMTs. After those repairs the data-taking period is called SK5. That is also the preparation period for SK Gd. It in started June 2018 and ran 2019 July.

Table 2.1: The summary of SK data taking periods.

	SK-I	SK-II	SK-III	SK-IV
Operation Start	Apr. 1996	Oct. 2002	Jun. 2006	Sep. 2008
Operation End	Jul. 2001	Oct. 2005	Sep. 2008	May. 2018
Livetime(days)	1489.2	798.6	518.1	3244.4
ID PMTs	11,146	5,182	11,129	11,129
ID PMTs	1,885	1,885	1,885	1,885
Photo coverage	40%	19%	40%	40%

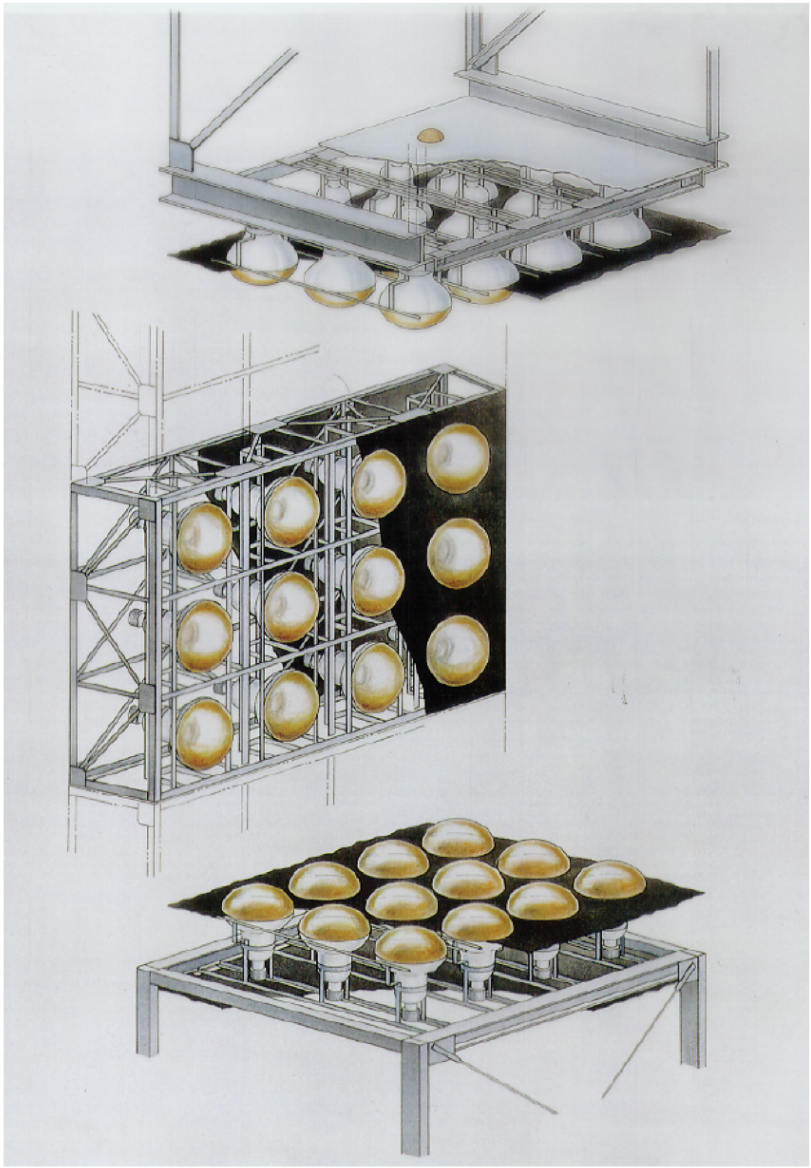

Figure 2.4: Frame structure that supports PMT. [67]

The SK-Gd phase is a big project to improve the SK performance. The Gd is means gadolinium is dissolved this ultra-pure water at SK. The gadolinium has a large cross-section to capture the neutron and emit 8MeV gamma rays. Therefore, it will make us identify the neutrino interaction which emit neutrons. This makes it easier to separate neutrino from antineutrino interactions. We will talk about the detail of how to separate the anti-neutrino and neutrino in the next chapter.

2.1.3 Cherenkov light

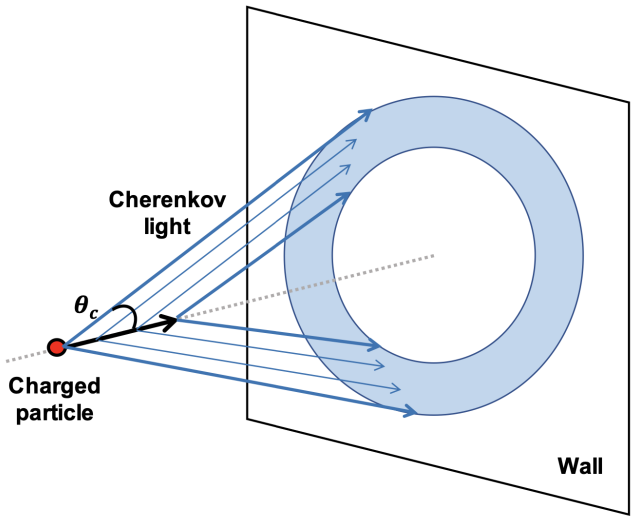

Figure 2.5: Outline drawing of Cherenkov light. [3]

The SK is designed for detecting the charged particles by using Cherenkov light. The Cherenkov light will happen when charged particles go through the dielectric medium faster than light in the medium. SK uses that nature to detect the charged particle when this particle has a higher speed than the light speed in the water. The Cherenkov light momentum threshold for differently charged particles is listed Table2.2. A visualization of the The Cherenkov light is shown in the Figure 2.4. We can find the Cherenkov light is just like a cone surrounding the charged particle. The cone direction is same as the charge particle

Table 2.2: The summary of Cherenkov momentum thresholds in water.

partilce type	mass(MeV)	threshold(MeV)
electron	0.511	0.57
muon	105.6	118
pion	140	156
proton	938	1051

direction. The opening angle of the cone is related to the speed of the charged particles. The relationship of this two parameter is like

$$\cos\theta_c = \frac{1}{n\beta}. \tag{2.1}$$

The θ_c is the opening angle, n is the refractive index of the medium, beta is the speed of charged particles divided by the speed of light in vacuum. The calculation of the momentum threshold is

$$p_{\text{thresh}} = \frac{mc\beta_{\text{thresh}}}{\sqrt{1-\beta^2_{\text{thresh}}}}, \quad \text{with} \quad \beta_{\text{thresh}} = \frac{1}{\text{n}}. \tag{2.2}$$

If beta is nearly to equal to 1, the opening angle is about 42 degree.

The spectrum of the Cherenkov light photon number by using the wavelength parameter lambda by following this formula

$$\frac{d^2N}{d\lambda dx} = \frac{2\pi\alpha}{\lambda^2}\left(1-\frac{1}{n^2\beta^2}\right). \tag{2.3}$$

The α is the fine structure constant. In SK PMTs have sensitivity to wavelengths from, 340 nm to 600 nm, and in this range are about 340 photons generated when one charged particle goes through 1cm. Using this nature, we can reconstruct the charged particle energy by accounting for the number of photons. But if the charged lepton has less energy than 400MeV, we could also use the opening angle to reconstruct the charged particle's momentum.

The PMT (photomultiplier) is the photon sensor that uses the photoelectric effect to transfer the photon to electron and multiply the electron. The standard step of how to transmit the photon signal to electron signal is like this way:

1. The photon enters into the PMT and then interectats with the dynode and generates the photoelectron.

2. The photoelectron is focused on the first dynode and interacts with it.

3. After the second photon electron has been generated. It will interact with the second dynode and generate more electrons.

4. Repeat the steps 2 and 3 several times. Then we get the charge current from the positive dynode.

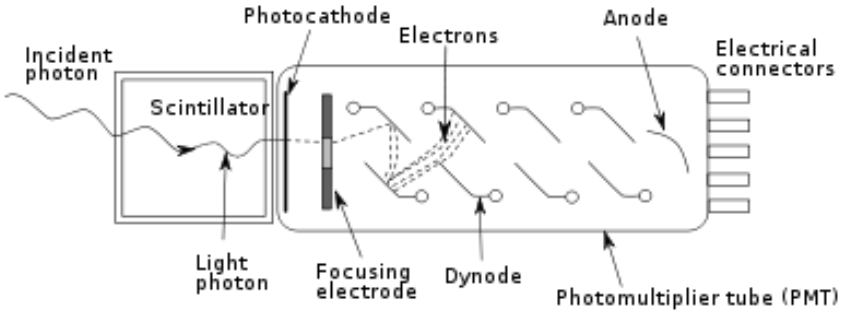

Figure 2.6: Schematic diagram of the operating principle of PMT [72]

Because the current is proportional to the number of entering photons, if we integrate the charge, we could get a total charge and estimate the number of incoming photons. Furthermore, if we do some calibration about the PMT, we could find the relationship of the photon number and the total charge, then we could estimate the energy of the charged particles.

There are two types of PMT installed in the SK. The first one is the 8-inch PMT that

was established in the OD [14]. The second one is the 20-inch PMT which is installed in ID. The 20-inch PMT is manufactured by Hamamatsu Photonics K. K. [42, 66]. Figure 2.6 shows the structure of 20 -inch ID PMT. The photocathodes, is made of Bialkali, a type of alloy containing Sb-K-Cs, and the quantum efficiency peaks at 22% percent at the wavelength of 390nm shown in Figure 2.4. And another performance parameter is summarized in Table2.3 [66].

As I have mentioned before, the earth magnet will have an impact on the time resolution of PMTs. Consequently, 26 sets of Helmholtz coils are installed around the water tank. The currents of the Helmholtz are monitored in real-time. The original magnetic field, which the SK group measured before SK1, is 450mG. After installing the Helmholtz coils, the magnet field is reduced to 32 mG. This value is less than 100mG. Beyond this value, the time resolution will increase significantly. [4]

Table 2.3: Specifications of the 20-inch ID PMTs. [66]

Photocathode material	Bialkali (Sb-K-Bs)
Quantum efficiency	22% at λ=360 nm
Dynode structure	11-stage Venetian blind type
Operation high voltage	1700-2000 V
Gain	10^7 at 2000 V
Dark current	200 nA at 10^7 gain
Dark rate	3 kHz at 10^7 gain with 0.25 p.e. threshold
Transit time	90 ns at 10^7 gain
Transit time spread	2.2 ns(1 σ)

Since learning the lessons of the PMT chain explosion in 2001, every PMT has been covered with a 12 mm ultraviolet transparent acrylic dome. On the side of the PMT is be protected by acrylic and fiberglass reinforced plastic (FRP). To make sure the pressure of the water is constant, the FRP is designed with holes to make sure the water could flow around the PMT. For the vertical photon with 3500nm wavelength, the acrylic dome trasparency is about 96%. [4].

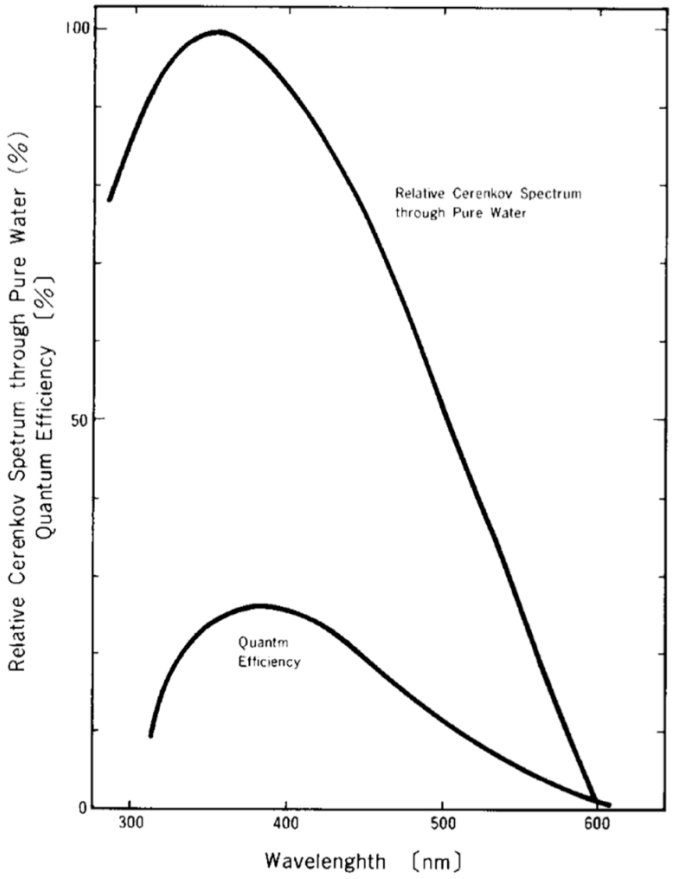

Figure 2.7: Quantum efficiency distribution of 20-inch PMT and relative Cherenkov light distribution when passing through 15 m of pure water. [66]

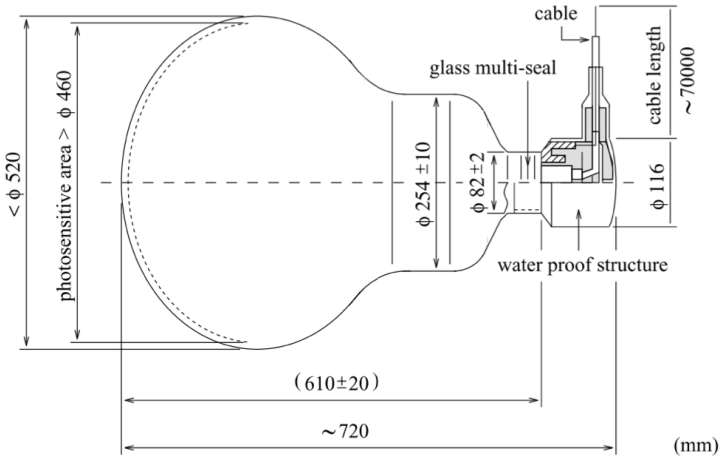

Figure 2.8: 20-inch PMT. [66]

2.2 Electronics and Data Acquisition

As mentioned before, the front-end electronics were upgraded for the SK4 period. The previous electronic circuit is called ATM for ID and ODQTC for the OD. For the SK4, it uses the QTC-Based Electronics with Ethernet, called QBEE [51].

The QBEE consists of two main parts, Charge-to-Time Converter (QTC) and the Time-to-Digital Converter (TDC). One QBEE connects to eight QTC, and one QTC connects to 3 PMTs. The workflow of the QBEE is like this. Initially, The charge of the PMT signal is integrated by QTC, and then the QTC output is converted to a digital signal by using the TDC. And then, this time and charge information is recorded by FPGA at 60kHz. Figure 2.9 shows the workflow detail.

The dynamic charge range for one QEBB is from 0.2 to 2500 pC [53], and each channel has three different gains, the relative ratios for divided channels is 1, 1/7,1/49, each of them corresponding to the large medium, and small gains. Show the detailed structure and the signal readout system and its surrounding equipment.

There are significant advantages for the QBEE compared with the previous front-end electronic system. In QBEE the current is discharged as constant current, just as the figure shows. Consequently, the output of QBEE gives time and charge information at the same time. That will decrease the dead time compared with the old electronic ATM.

And another upgrade is the trigger. Previously, there was only a hardware trigger in the SK. After that, SK4 used the software trigger and the SLE, LE, and HE triggers. We should note that there should be two particular triggers: the Super High Energy (SHE) and the after trigger (AFT). This trigger is associate with the neutron targeting system. And the neutron information will help us to distinguish the anti-neutrino and neutrino. We will describe this a little later.

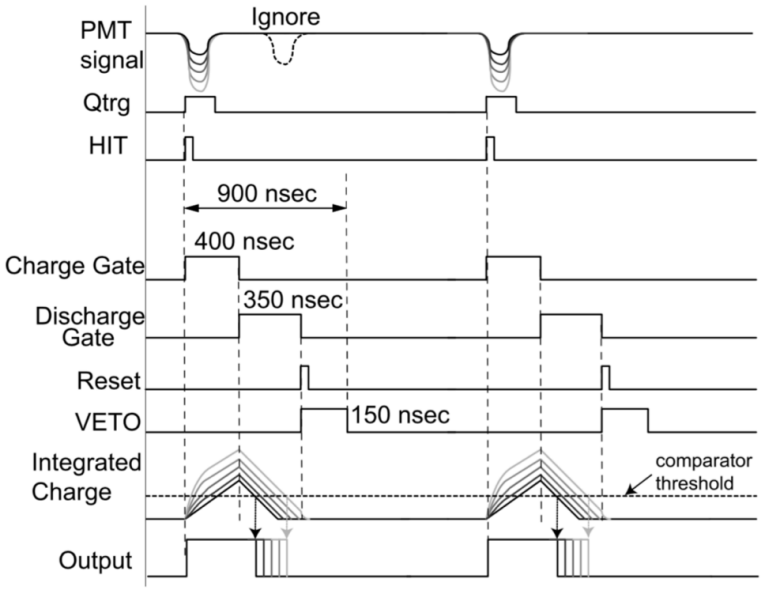

Figure 2.9: Timing chart of QTC operation QBEE for SK-IV. From [51]

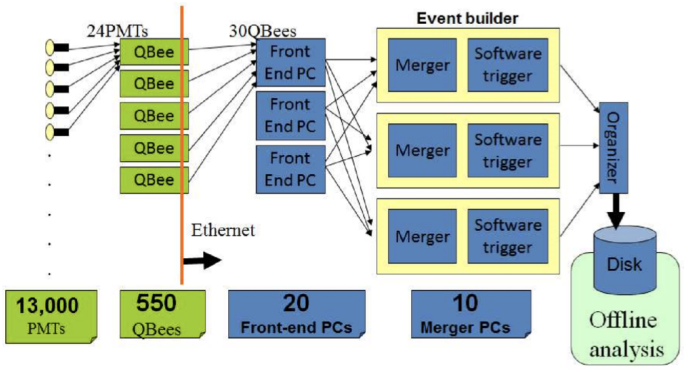

Figure 2.10: Block diagram of data collection system until PMT signal is recorded on disk From. [74]

2.3 Water and Air Purification

The SK water uses underground water from the Kamioka mine. However, it is important to keep water high transparency to ensure the light will not be absorbed or scattered. Furthermore, radioactive material, like the radon, comes from bedrock and dissolves into the water.

It will become the main background of the solar neutrino measurement. For this reason, we apply the water purifier system in the SK. The water flow of SK is about 60 tons/hour, and the water used in SK is recycled water. There is also a heat exchanger system installed in the water system to keep the water temperature in 13.6 degrees. This helps to prevent the bacteria from reproducing in the tank, and reduces the dark rate of the PMT.

Apart from the purified water system, an air purifier system is also installed in the SK. Because the radioactive material in the air may be dissolved into the water and become another background for solar neutrino measurement, we install the air purifier system to pump the radon-free air into the SK tank.

Chapter 3

Event Reconstruction

The event reconstruction algorithm used in SK is called APFit. The APFit could use the time information, the charge information, and the PMT positions to derive the physics information for every Cherenkov ring signal, such as the direction, momentum, particle identification. The APFit is applied to the Monte Carlo simulation generated in this analysis and SK data. I will introduce some of the basic ideas of the APFit. If you interest in the detail of the APFit, please check this paper [62].

The reconstruction algorithm flow is like these steps.

1. Vertex fitting

2. Ring Counting

3. Particle Identification

4. Momentum Reconstruction

5. Michel Electron Finding

6. Neutron Tagging

We should note that the neutron tagging step is only used for SK-IV MC data since there is no AFT applied in the other SK periods.

3.1 Vertex Fitting

The vertex fitting has three steps. The first one is the point fit, then will be ring edge search and TDC fit. Initially, APFit assumes that the charged particle generated all of the Cherenkov light from one point, then it will calculate the time residual ((the photon arrive time)-(the photon propagate time in the water)) as the fit parameter to find the peak. The goodness of the fit is defined as follows.

$$G = \frac{1}{N}\sum_{i} \exp\left(-\frac{(t_i - t_0)^2}{2(1.5\sigma)^2}\right). \tag{3.1}$$

Here N is the number of hit PMTs, t_i is the time of flight meanwhile subtract the PMT timing, t_0 is the fit time to maximize the good, and the σ is the PMT timing resolution, about 2.5 ns. After the Point Fit stage, the APFit will estimate the direction and the opening angle of the Cherenkov ring. The opening angle $\theta_{edge}$is defined satisfied

$$\frac{d^2\mathrm{PE}(\theta)}{d^2\theta} = 0 \tag{3.2}$$

Where $PE(\theta)$ is the angular distribution of the observed charge by using the opening angle as function parameter. Figure 3.1 shows the distribution for PE and theta.

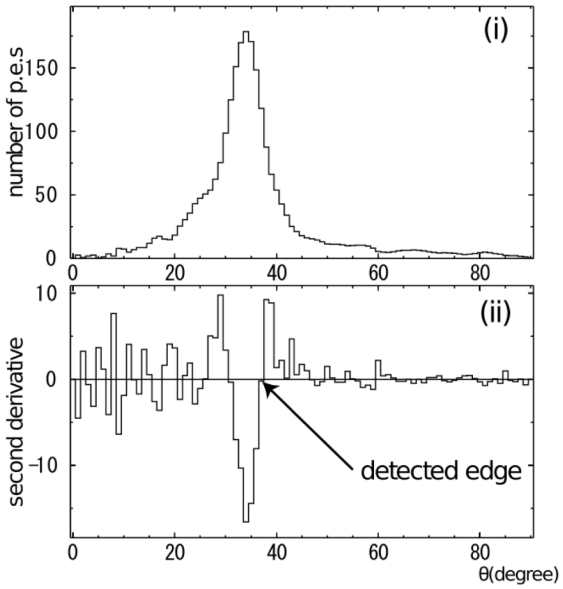

Figure 3.1: An observed charge distribution as a function of Cherenkov opening angle (top) and its second derivative (bottom). [51].

And the direction of the Cherenkov light is estimated using:

$$Q\left(\theta_{\text{edge}}\right) = \frac{\int_0^{\theta_{\text{edge}}} \text{PE}(\theta)\text{d}\theta}{\sin\theta_{\text{edge}}} \times \left(\left. \frac{d\text{PE}(\theta)}{d\theta} \right|_{\theta=\theta_{\text{edge}}} \right)^2 \times \exp\left(-\frac{\left(\theta_{\text{edge}} - \theta_{\text{exp}}\right)^2}{2\sigma_\theta^2} \right). \quad (3.3)$$

The θ_{exp} is the expected Cherenkov light opening angle calculated from the total charge inside of the θ_{edge}, the σ_θ is the angular resolution. Initially, The Q will use the point fit direction, and then it will calculate the different directions to choose the maximized Q.

Finally, APFit will recalculate the vertex position by using the directional and opening angle information above. This recalculation will not assume the Cherenkov light generated from one point. Instead it will consider all photons originated along the charged particle track length, about 3MeV per cm, to get the residual PMT time mentioned before. Then APFit will maximize the likelihood function. The scattering of Cherenkov light is also considered here.

3.2 Ring Counting

From now we have identified the main ring. Other rings are searched by using a pattern recognition algorithm called Hough transform [17]. Here is the basic idea of Hough transform. Initially, The APFit will assume a virtual ring pattern for very hit PMT. The virtual ring will be weighted by the charge information from the hit PMTs. APFit will identify the actual ring from the peak of the overlapping virtual distributions. Just like the Figure 3.2 shows. In practice, APFit will implement all of the charge distribution functions from every hit PMT, then identified the real ring by finding the peak in the overlapping distributions. There is a log-likelihood method used to determine the actual ring.

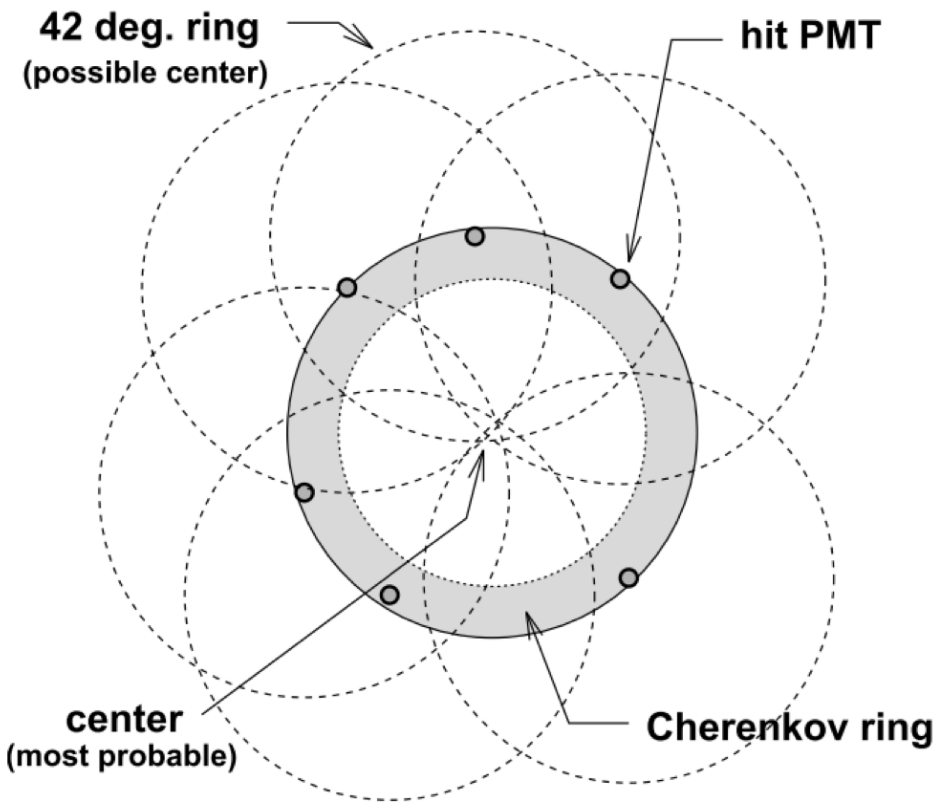

Figure 3.2: An outline drawing of detecting additional rings. The shaded and dashed circles stand for the Cherenkov ring and rings with 42^o half angles [51].

3.3 Particle Identification

The charged particle identification in SK classifies events into two categories. The first one is the e-like event which will contain the electron, positron, and gamma rays. This pattern event will produce a fuzzy ring due to the scattering and electromagnetic shower (bremsstrahlung with the pair production). Another is the muon-like event. This type of event will have a clear edge ring. The heavier particles will not be scattered so much. The comparison of this two type of the event is illustrated Figures 3.3 and 3.4.

The reconstruction particle identification algorithm identifies the event type by considering the charge distribution function from MC simulations. The likelihood test will be used for the identification to determined which type of event is seen, just like the figure shows. The quality of the PID algorithm is checked by using a one kiloton water Cherenkov Detector with electron and muon beams generated from the 12GeV synchrotron at KEK.

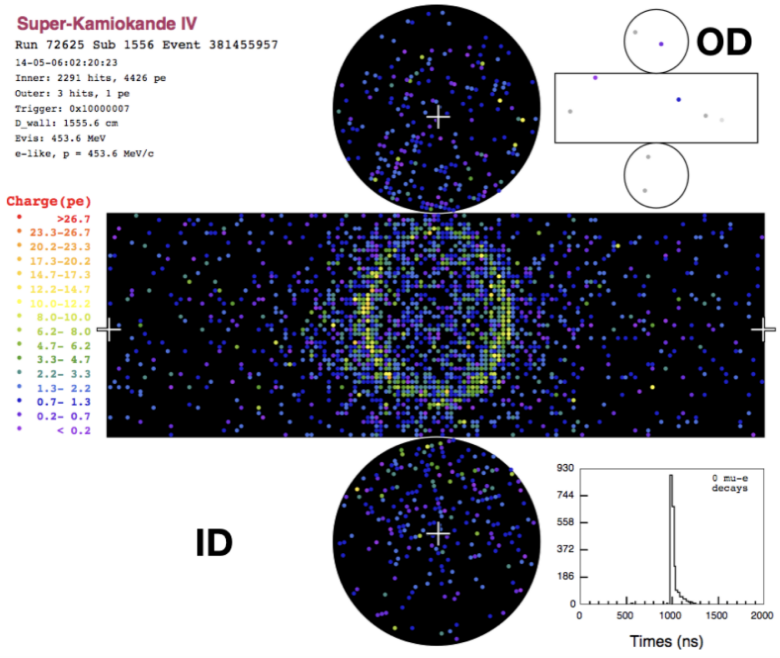

Figure 3.3: Typical e-like ring pattern.

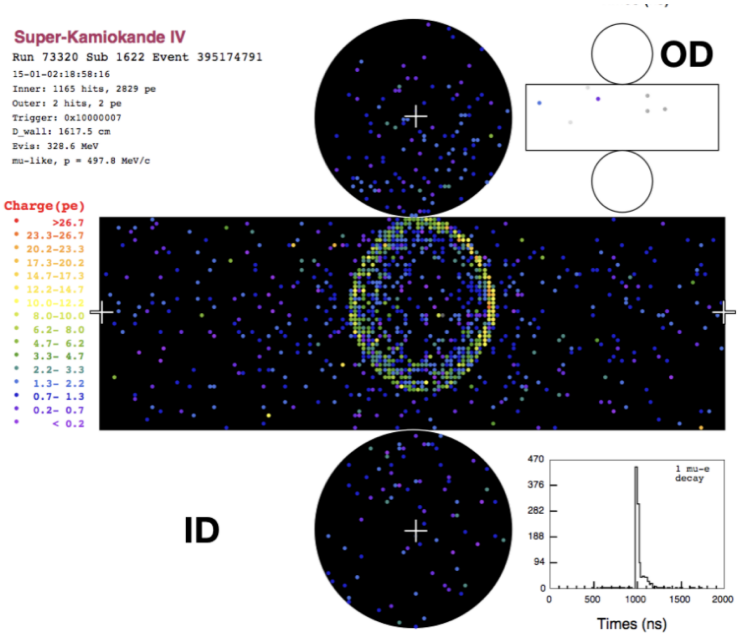

Figure 3.4: Typical μ-like ring pattern

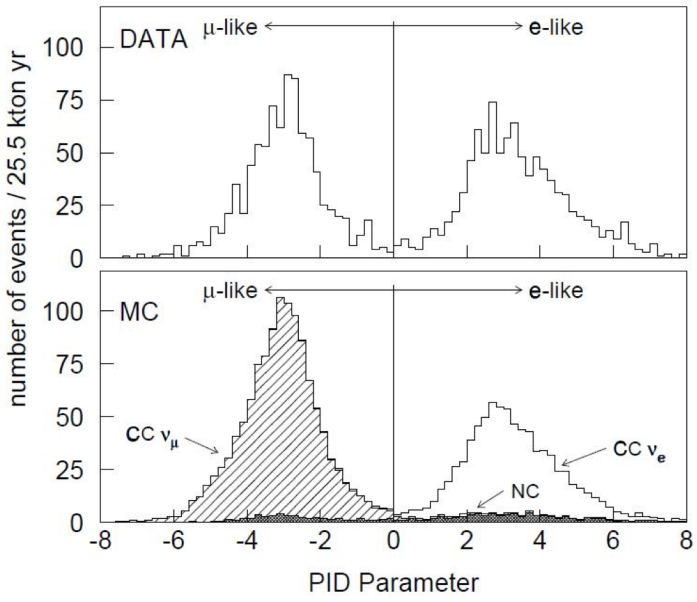

Figure 3.5: PID likelihood distribution for data and atmospheric MC with a visible energy below 1.33 GeV. Good separation between e-like and μ-like events is seen. [62].

3.4 Momentum Reconstruction

The momentum of each ring is calculated from the integrated charge within a 70 degree cone around the reconstructed ring direction. The integrated charge for number of n ring, R is given by:

$$R^n_{TOT} = \frac{G_{\mathrm{MC}}}{G_{\mathrm{Data}}} \left(\alpha \sum_{\theta_{i,n}<70^\circ} \left(q^{\mathrm{Obs}}_{i,n} \, \mathrm{Exp}\left[\frac{r_i}{L}\right] \frac{\cos\omega_i}{f\left(\omega_i\right)} \right) - \sum_{\theta_{i,n}<70^\circ} S_i \right). \tag{3.4}$$

Here, variables are α: the normalization factor

G: the relative PMT gain parameter for Data and MC

θ: the opening angle between the n ring and the PMT direction

$q^{\mathrm{Obs}}_{i,n}$: the integrated charge for the i PMT from n ring

t_i: residual time for I PMT

L: attenuation length in water

r_i: the distance from the vertex to the PMT

$f(\omega_i)$: PMT acceptance correction as a function of incidence angle ω_i

S_i: the expected amount of p.e.s from scattered photon s for the i PMT

When we finish, calculate the R^n_{TOT}, the corresponding ring momentum is determined by using a correspondence table built from MC. The Figure 3.6 shows the correspondence of three particle types.

The reconstructed momentum resolution for single ring event is estimated to for electron and 3% for muons.

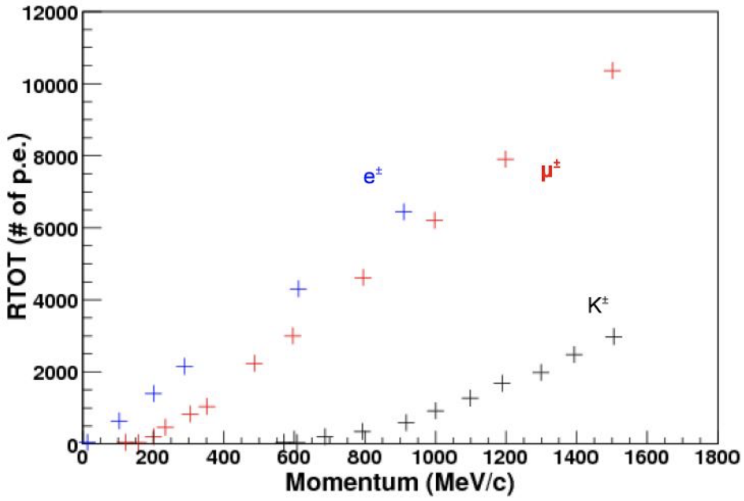

Figure 3.6: RTOT vs. momentum table for the electrons (blue crosses), muons (red crosses) and the kaons (black crosses). [40]

3.5 Michel Electrons Reconstruction

The Michel electrons from muon decays are a piece of essential information to determine if a charged particle is muon or not. There are two different Michel electron types in SK. The criteria for selecting a Michal electron is:

1.The time interval to the primary event is $1.2\mu s<\Delta t<20\mu s$ or $0.1\mu s<\Delta t<0.8\mu s$

2. Number of the PMT is > 50

3. Vertex is well reconstruct

4.Total p.e.s < 2000

5. Number of hit PMTs in 50 ns window is > 60

6. Number of PMTs in the 30 ns window is > 40

The last two criteria are aimed to reduce the gamma-ray emitted when the oxygen nucleus captures a muon. More Michel electrons are observed from positive muons since negative muons often capture on oxygen nuclei.

3.6 Neutron Tagging

When a neutrino interacts with the nucleus in the tank, some neutrons may be produced. The number of the neutron will be different by different lepton interact with the nucleus. Therefore, the neutron will be an essential part of distinguishing additional lepton.

The neutrons will finally capture on the hydrogen nucleus and emit de-excitation gamma-ray when traveling in the water. The gamma rays' energy is fixed, about 2.2 MeV, and the mean capture time is about 204.87μs. These two pieces of information could help us to tag neutrons.

Here I will introduce some basic ideas of the neutron tagging algorithm used in SKIV. If you interest in the detail of this technology, please check [36],[47].

Firstly, we reject the event which has two PMT hits within 10 μs, due to this type of event might be the dark noise papers in PMTs in very high possibility. Then, we search for candidate hit cluster with 2.2 MeV gamma-ray. Finally, we put this candidate into 16 variables, which represent the characteristics of the cluster. The neural network is used determines if this cluster is the 2.2 MeV gamma-ray cluster or not. Currently, the neutron efficiency is 25.2% with a mistagging rate is 1.8%.

Chapter 4

Event Simulation

The neutrino event in the Super-Kamiokande is simulated by the Monte Carlo method. This simulation consists of three parts: the estimated neutrino flux, the neutrino interaction, and the particle propagation simulation in the Cherenkov Detector.

For the first part of this simulation, the neutrino flux estimate is already calculated by the theorists. [35] They estimated monogenic neutrino would have an energy of about 459 MeV. We will introduce the detail of this analysis in section 4.1.

And the background of this analysis mainly comes from the atmospheric neutrino since the solar neutrino is too small (smaller than 10 MeV) to be accountable. The atmospheric neutrino flux is modeled with the Honda Flux, calculated by M. Honda et al.[33, 30, 31, 32] We will describe the detail of the atmospheric in section 4.2.

The neutrino interaction software used in SK is NEUT [46, 29]. NEUT could generate the secondary particles after the neutrino interaction and the related physics information, such as momentum, direction. After the NEUT simulate the interaction of neutrinos, the secondary particles propagate in the water, and the scattering will be simulated by SKDETSim,

a GEANT3 based Monte Carlo simulation software. And the track will finally be recorded in electronics simulation by using SKDETSim too.

4.1 Monogenic Neutrino Simulation

To estimate how many high energy neutrino would arrive at the SK, we should account for the astrophysical monopole abundance at first. Using the primary constraint from the Parker bound, the Galactic magnetic field constraint, the monopole flux limit is [27]

$$F < 10^{-15} \left(\frac{B}{3\mu\mathrm{G}}\right) \left(\frac{r_G}{30\mathrm{kpc}}\right)^{1/2} \left(\frac{300\mathrm{pc}}{\ell}\right)^{1/2} \left(\frac{30\mathrm{Myr}}{\tau_G}\right) \mathrm{cm}^{-2}\ \mathrm{s}^{-1}\mathrm{sr}^{-1}. \tag{4.1}$$

Here the F_m is the bound of the monopole flux, there is a more strict bound by estimate the monopole catalysis of the neutron decay from the neutron star. However, this result has a sizeable systemic error from neutron star structure since the physics in the neutron star is still unknown. Apart from this, some theorists suggest that the co-annihilation processes might reduce these monopole flux from the Parker bound [43].

We could estimate the total number of captured monopoles by using the age and size information of the Sun. In general, we should account for the monopole velocity and the corresponding energy loss inside the Sun. After that, we could estimate the monopole capture fraction in the Sun. It is already estimated that capture fraction of 10^{16} GeV GUT monopoles is almost one, and the number of monopoles captured in the Sun is approximately $N_M \sim 10^{41} F_M$ [22], which is the astrophysical monopole abundance.

As mentioned before, the total monopole number captured by the Sun may be suppressed by the co-annihilation processes. If we consider this effect, the number of captured

monopoles should be estimated to $N_M \sim 10^{33} (F_M)^{1/3}$ [32]. However, a significant source of uncertainty comes from the nature of the magnetic field in the stellar interior, since the magnetic field could separate monopoles and anti-monopoles. Then, it would prevent annihilation. Furthermore, even if these processes occurred, we still couldn't estimate the timescale associated with the annihilation process. In principle the monopole anti-monopole annihilation cross-section should be set by the GUT scale. Therefore, their co-annihilation rates could be negligible for our analysis. If you interest in the monopolonium state, you can get more information in [22].

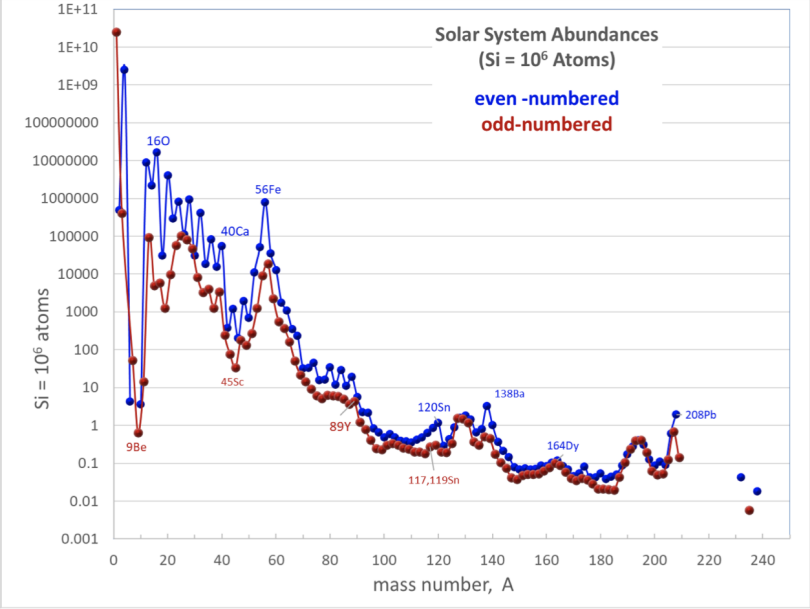

Figure 4.1: Abundances of the isotopes in the Sun as a function of mass number. Even numbered nuclides are shown in blue, odd-numbered nuclides in red. [44]

Therefore, our analysis is based on the 459 MeV monoenergetic antineutrino search, which offers better discovery potential than the indirect decays. Since co-annihilation will affect both direct and indirect processes equally, we don't consider this effect in our analysis unlike previous monogenic neutrino search in SK [68]. Therefore, we don't struggle with the swamp of the detailed classification of monopole physics. We take it in a phenomenological and straightforward way called,' bottom-up' approach for the rest of the analysis [8].

After considering the abundance of magnetic monopoles, we should estimate the momentum spectrum of proton decay neutrinos. If we ignore the binding energy brought by the nuclear structure, the energy of the decaying neutrino should be limited to 459 MeV. However, this is an advantage of this research, that is our research object is the Sun, and we could conclude from the figure that the Sun's interior is mainly composed of hydrogen and helium and their isotopes. For hydrogen, we can regard them as a free proton. Furthermore, the nuclear binding energy per nucleus is 7.1 MeV for helium. The binding energy is too small to be comparable with the momentum of the decaying neutrino, not to mention to compared to other systematic errors. Therefore, as shown in Figure 3.1 below, we assume that the momentum spectrum of the decaying neutrino is an average distribution with the center value of 459MeV.

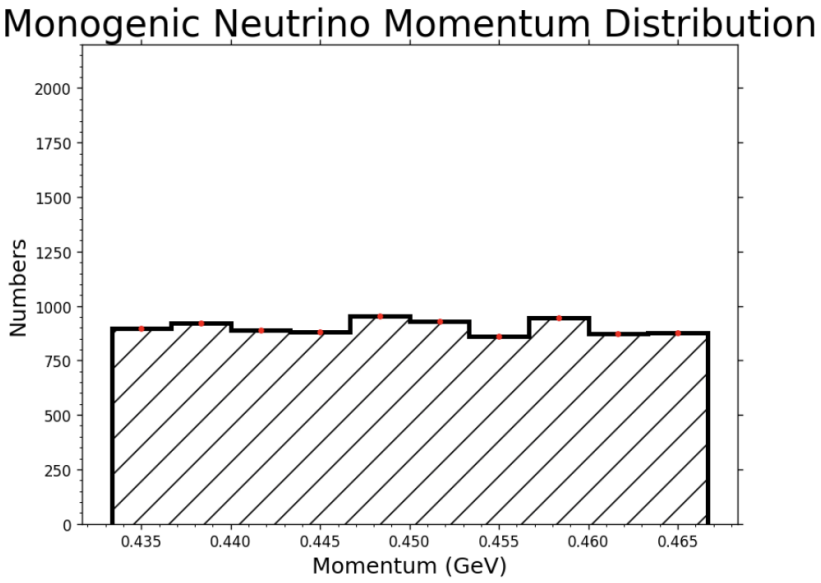

Figure 4.2: Monogenic Neutrino Momentum Distribution, assuming 20,000 monopole neutrino is generated by MC.

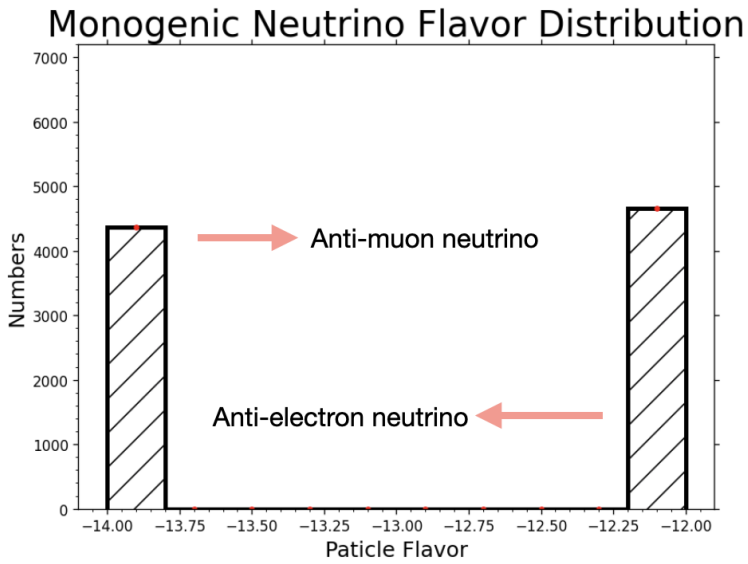

Figure 4.3: Monogenic Neutrino Flavor Distribution, assuming 20,000 monopole neutrino is generated by MC.

4.2 Atmospheric Neutrino Flux

The main background for monogenic proton decay searches comes from the atmospheric neutrinos produced by cosmic rays since the atmospheric neutrino has a wider momentum spectrum and a higher event rate than the monogenic neutrino.

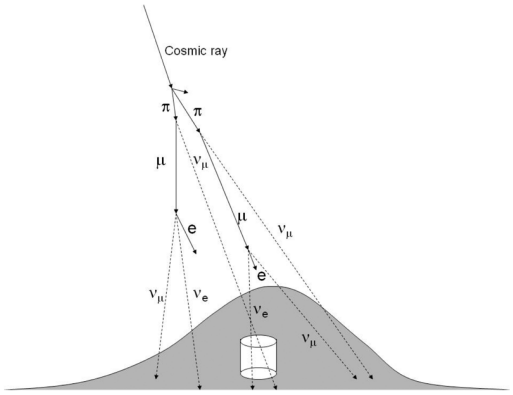

Figure 4.4: Schematic view of cosmic ray interactions in the atmosphere. [45]

The cosmic rays, which could strike the atmosphere, are the mainly protons and α-particles. The cosmic rays interact with the atmosphere nuclei isotropically. This interaction will produce several pions and kaons. The charged pions will decay into a muon neutrinos (ν_μ or $\bar{\nu_\mu}$) and one muon. Then, the muon will decay into one electron and an electron neutrino. It could make us estimated the neutrino flux composition at the surface of the Earth. If we only consider the pion decay, the ratio of the ν_μ and ν_e should be 2. However, there is another decay mode after the comic ray interacted with the atmosphere nuclei, as the Table is shown. Therefore, the ratio of the ν_μ and ν_e will be different with 2, just as the figure 4.5 showed. The detail of the reaction chain is shown in Figure 4.4. However, most of the neutrinos pass through Earth without any interaction. Only a little part of neutrino will interact at Super-Kamiokande. The observed neutrino event rate in SK is eight events/day.

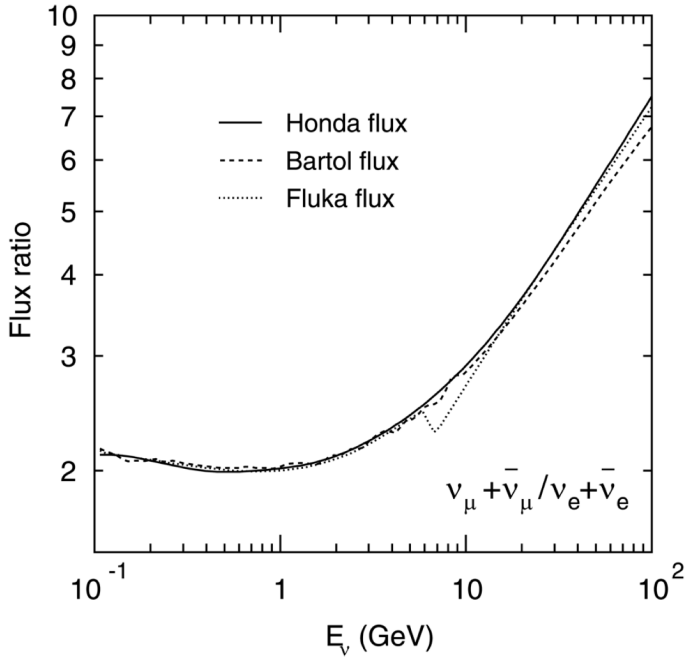

Figure 4.5: Calculation of the neutrino flux ratio $(\nu_\mu + \bar{\nu_\mu})$ / $(\nu_e + \bar{\nu_\mu})$to the energy of atmospheric neutrinos by the group [7]. The solid line is from Honda, the wavy line is from Bartol, and the dotted line is from Fluka.

The detail of the Honda flux is shown in Figure 4.5. This flux model will calculate the

cosmic rays through the atmosphere in three dimensions. Furthermore, it will also account for the effects of the geomagnetic field and solar wind, which could affect the cosmic ray flux by a factor of 2% at 1 GeV and a factor of 10% at 10 GeV. The interactions with the air nuclei are using NUCRIN and DPMJET-III [59] models, with secondary particle information of mesons and kaons calculate by neutrino flux computation. Neutrino flux calculations by G.Battistoni et al. (Fluka flux) [12], and G.D. Barr et al. (Bartol flux) [11] are used for comparison with Honda flux, as shown in Figure 4.5. Flux calculations cover the neutrino energy ranging from 30 MeV to 3 TeV.

4.3 Neutrino Interaction

The atmospheric neutrinos nucleons interaction, which happened in the SK tank, are simulated by NEUT [46, 29]. The interactions mode of the atmospheric neutrino MC events are divided into two catalogs, the Charged Current (CC) and Neutral Current (NC):

CC/NC elastic and quasi-elastic scattering $\nu + N \rightarrow l + N'$

CC/NC single meson and gamma production $\nu + N \rightarrow l + N^*$ $N^* \rightarrow N' + (\pi, K, \eta, \gamma)$

CC/NC deep inelastic scattering $\nu + N \rightarrow l + N' +$ hadrons

CC/NC coherent pion production $\nu + {}^{16}\mathrm{O} \rightarrow l + {}^{16}\mathrm{O} + \pi$

where the ν is a neutrino, N and N^* are the initial state and final state for nucleons, and l is a lepton (neutrino for NC and charged lepton for CC interaction). The distributions for the simulated cross sections of neutrino interactions in NEUT are shown in Fig. 4.6.

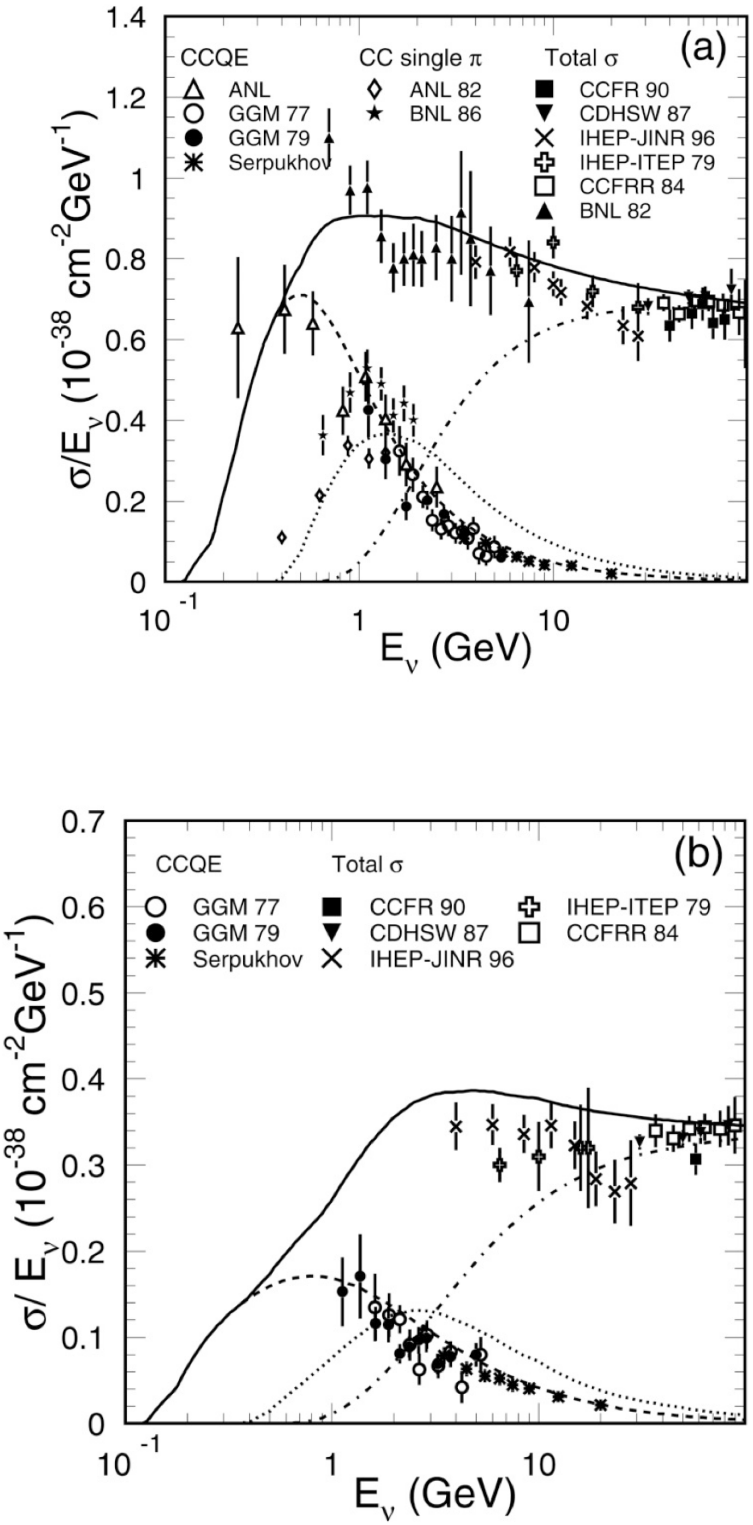

Figure 4.6: The simulated cross sections for $\nu(\bar{\nu})$ interactions in NEUT with data. The red, blue, green, and black solid lines correspond to (quasi-)elastic scattering, single π K, η, γ production, deep inelastic scattering, and the total of three interactions. [36]

4.3.1 CC/NC elastic and quasi-elastic scattering

The NC elastic scattering interaction is a neutrino is scattered by a nucleon without generating any particle.

$$\nu + N \rightarrow l + N'. \tag{4.2}$$

For the interactions in bound nucleons in 16O, the Smith and Moniz model is applied, which treats the nucleus by using the Fermi gas model with a flat momentum distribution up to 225 MeV/c (Fermi surface momentum). However, the CC quasi-elastic scattering interaction (CCQE) is a neutrino that converts into a corresponding charged lepton. The CCQE cross-sections for free protons are calculated given by Llewellyn-Smith model [39] in the simulation. Additionally, the model note [50, 49] is also accounted to provide the systematic error of the bound nucleon scattering. The Pauli exclusion principle is evaluated by [65] when the scattered nucleon momentum is higher than the Fermi surface momentum.

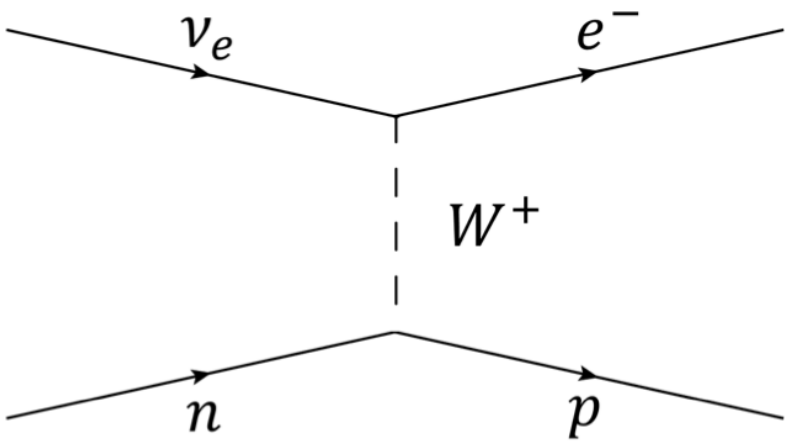

Figure 4.7: CCQE reaction by ν_e

The relationship of the cross-section of NC elastic scattering and the cross-section of CC elastic scattering are estimated by [7, 2]: And the comparison of the NEUT calculated

cross-sections of CCQE scattering with experimental data is shown in Figure 4.8..

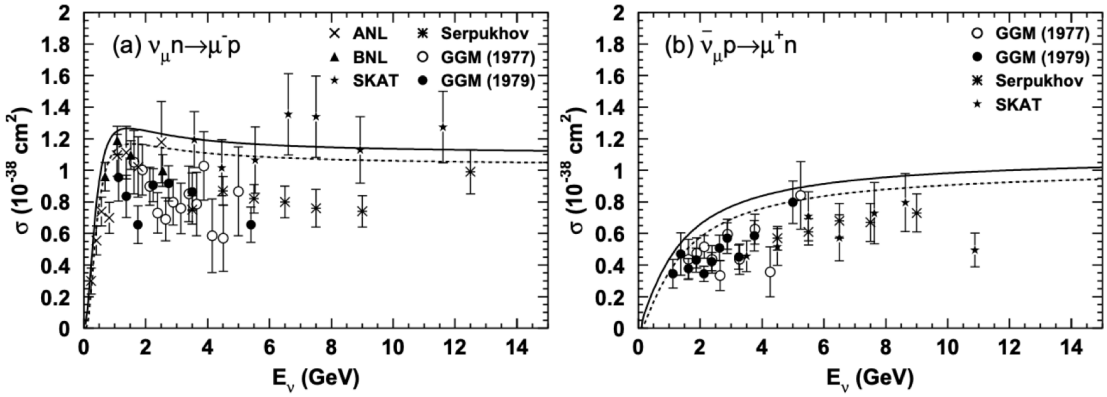

Figure 4.8: Calculated cross-sections of CCQE scattering with experimental data as the function of neutrino energy. The solid and dashed lines show the calculated cross-sections for free and bound targets. [29]

4.3.2 CC/NC single meson and gamma production

Single meson, such as π K, and η and a γ-ray can be produced by the nucleon resonance state N^*:

$$\nu + N \to l + N^* \tag{4.3}$$

$$N^* \to N' + (\pi, K, \eta, \gamma) \tag{4.4}$$

Single-meson production of π K and η are simulated by using the Rein and Sehgal model. [57, 56] There is a total of 28 resonances are considered in SK simulations. The final state pion angular distribution could be derived from the $\Delta(1232)$ resonance. The angular distribution of pions coming from other resonances is assumed to be isotropic. This angular distribution is derived by the experimental data from $\nu p \to \mu^- \pi^+ p$ scattering [41]. Pion-less Δ decay [63] is also simulated. As before, the Pauli exclusion principle is accounted, when the scattered nucleon momentum is greater than the Fermi surface momentum.

4.3.3 CC/NC coherent pion production

Neutrinos could interact with oxygen nuclei with a charged pion production. The pion is transferred from the oxygen nucleus. The pion is emitted in the same direction with the neutrino and carries little momentum, given by the oxygen nucleus. This interaction mode is called the coherent pion production, and the Rein Sehgal model has also stimulated it [57, 56].

4.3.4 CC/NC deep inelastic scattering

If the neutrino energy is higher than 10 GeV, the deep inelastic scattering will become the dominant neutrino interaction mode. Neutrinos could interact with a quark in a nucleon and produce multiple hadrons in such high energies regions. The cross-section of deep inelastic scattering has been calculated by using the GRV98 (Gluck-Reya-Vogt) Parton distribution function [26]. In the energy region of W<2.0 GeV/c^2, we only consider the pions as produced hadrons, and its multiplicity is estimated from the results of BEBC experiment [48](and bubble chamber experiments [18]). When the energy of neutrino at the region of W>2.0 GeV/c^2, the PHYTIA/JETSET simulation package [64]is used to determine the hadronic system kinematics, and the productions of K and η mesons are also treated in the region.

Full MC simulation and data comparison of neutrino cross-section is shown in Figure 4.6. We could find that the simulations describe the data well.

4.4 Detector Simulation

As I have mentioned before, the particle propagation in water, Cherenkov photon emission, and the response of PMTs and electronics are simulated by SKDETSim, a GEANT3 based

simulation package.

The Cherenkov photon propagation has been simulated by considering the Rayleigh scattering, Mie scattering, and absorption by H_2O molecule. The Rayleigh scattering, only caused by small particles, which r $\ll \lambda$, the r is the radius of a particle. And the Rayleigh scattering will be the dominant scattering when photons have relatively short wavelengths of ($\lambda \leq 450$ nm). The scattering coefficient dependence of λ^{-4}, so that the photons will be scattered symmetrically in the forward and backward directions.

And for longer wavelength ($\lambda \geq 450$ nm), the dominant scattering process is the absorption by H_2O molecule. Besides, the Mie scattering is caused by large particles (r $\gg \lambda$) to scatter photons. And the Mie scattering is more intensely in the forward direction. Calibration data tune these scattering effects.

Chapter 5

FC Reduction

Approximately 10^6 events/day are collected by Super-K. We must separate the data relevant for physics studies from the background event, which is composed of low energy radioactivity events (e.g., radon) and cosmic ray muon events. Additionally, We must also remove the "flasher" events caused by the PMT dynode discharge. Below, we provide an overview of the automated "data reduction" algorithm for the fully contained (FC) data sample. This type of sample means it deposited all of its energy to the ID volume. This sample is the relevant sample for our monogenic neutrino search. If you interest in the details of the FC data reduction, as well as the decrease for the upward-going muon (UPMU) and the parts, contained (PC) data samples, you could check the [9, 58]. Figure 5.1 schematically shows different types of events in SK.

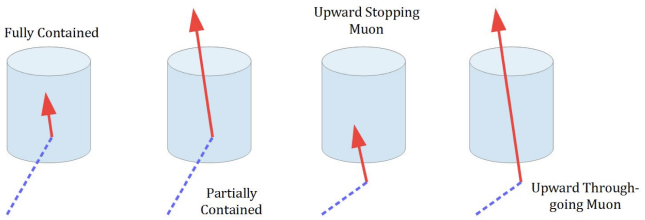

Figure 5.1: Schematic representation of the fully contained, partially contained, upward-going stopping and through-going muon event classes at Super-K.From [73].

5.1 The First Reduction

There are approximately 10^6 events triggered in SK per day. Most of them are downward cosmic ray muons signals and low-energy radioactive signals. To remove this background, the following reduction is given as the first step in FC event selection.

1. $\mathrm{PE}_{300} \geq 200$ p.e.s

The total number of observed photoelectrons PE_{300} within the time width of 300 ns in the inner water tank should be more than 200 photoelectrons (p.e.s).

2. $\mathrm{NHITA}_{800} \leq 55$

The number of hits in the outer tank within $\pm$ 400 ns, NHITA_{800}, should be less than 55.

The first condition corresponds to a threshold of approximately 22 MeV/c for electron momentum, which cuts most of his low-energy events such as radiation background. The second condition is set for cutting cosmic-ray muons that pass through the outer water tank. After this reduction, the event rate reduced from 10^6 events/day to about 3000 events/day.

5.2 The Second Reduction

The following reduction is given in the second stage FC event selection.

1.$\mathrm{PE}_{max}/\mathrm{PE}_{300} \leq 0.5$

The ratio of the most significant number of photons PE_{max} divided by the total observed ID PMT hits PE_{300} should be less than 0.5.

2. $\mathrm{NHITA}_{800} \leq 25$ (30 for SK-IV) or $\mathrm{PE}_{tot} \geq 100{,}000$ pes ($\geq 50{,}000$ pes for SK-II)

The number of 1 hits in the OD tank NHITA_{800} is less than 25, or the total number of photoelectrons in the inner tank PE_{tot} is more than 100,000.

The first condition can cut the event of the electrical noise of the PMT, which is observing a substantial signal compared to the surrounding PMT. The second condition is used to the cosmic ray muons, which are remaining after the first reduction. After this reduction, the event rate will be about 600 events/day.

5.3 Third Reduction

This reduction is used to remove much remaining background. The list of targets is shown here.

• Hard muon cut

A cut for cosmic ray muons with very high energies above 1 TeV.

• Cut of passing muons

A cot of muon events which whose entry and the exit point is very near in the OD tanks.

• Stop muon cut

It cuts cosmic-ray muons that enter from the OD detector and stop in the ID tanks. In this case, we could see there is an OD signal only.

• Cable hole muon cut

When the cosmic ray muon passes through a cable bundle connected to the PMT, the

bundle will block the Cherenkov light. Therefore, it seems that this muon enters their tank without leaving a hit. To remove this muon, 2 m $\times$ 2.5 m plastic scintillators are attached to the top of the cable hole. If this event is satisfied this condition, it will be cut. The first and second event reduction cannot remove this muon.

– There is a hit in the plastic scintillator

– Reconstruct event point is within 4 m region of the plastic scintillator.

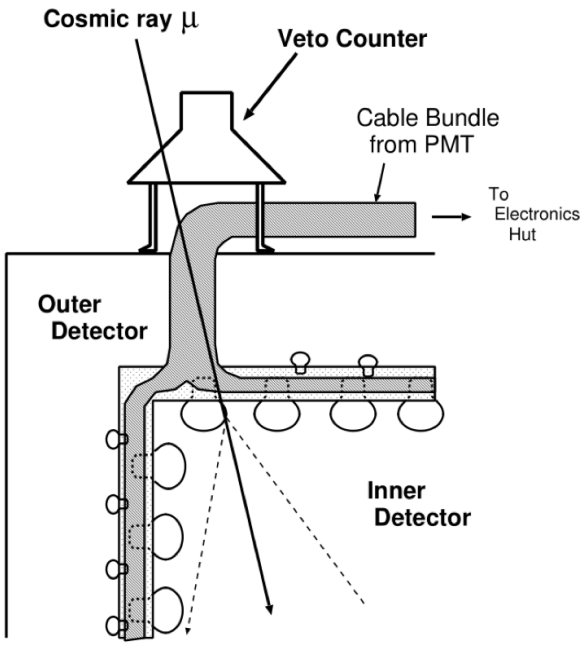

Figure 5.2: Schematic figure of Cable hole Muon and VETO counter [37].

• Coincidence muon cut

If a cosmic ray muon event accidentally overlaps with a low-energy event in the OD, the hit timing of the outer water tank will shift. We must remove such an event.

• Flasher event cut

Light emission may occur to the discharge of a PMT. This event is called a flasher event. The hit pattern of the ID identifies this background.

- Cut low energy events

After this reduction, the event rate will be about 50 events/day.

5.4 The Fourth Reduction

The fourth reduction is set up to remove the flasher event that the third could not remove since the flasher events will repeatedly have similar patterns. Therefore, we divide the ID tank into 1450 regions of 2 m $\times$ 2 m square, then the correlation r between the events could be calculated by the following formula.

$$r = \frac{1}{N}\sum_{i=0}^{N}\frac{\left(Q_{A,i} - \langle Q_A\rangle\right)\left(Q_{B,i} - \langle Q_B\rangle\right)}{\sigma_A \sigma_B}. \tag{5.1}$$

Here, $Q_{A,i}$, $Q_{B,i}$ are the photoelectrons number of the events A and B in the region i, $\langle Q_A\rangle$, $\langle Q_B\rangle$ are their mean values, and σ_A, σ_B are their standard deviations. When the correlation between the two events exceeds the threshold and the hit patterns are similar to the flasher mode, The event will be cut.

5.5 The Fifth Reduction

The 5th reduction consists of:

The remaining background events are targeted and removed in the fifth reduction. After this reduction, the event rate becomes about 30 events/day.

1. OD PMT hits in 200ns $\leq$ 10.

This condition aims to reject "invisible" cosmic-ray muons below the Cherenkov threshold but have an observed decay-electron.

2. cut the cosmic ray muon by using a more precise fitter

The list of the cut muon is as follows:

• Stop muon cut

• Cable hole muon cut

• Coincidence muon cut

• Longtail flasher event cut

• Electronics events

Cut fake hits coming from the noise of high voltage systems and electric boards.

• Dead electronics hut

Cables and electric boards from the PMT are concentrated in the electronics hut located at the top of the tank. If the electronics hut are not working correctly, there could be some fake hit.

• Calibration event cuts. If the data contains laser events used to calibrate the detector, it will be cut.

5.6 The Final Reduction

The final reduction is shown as follows:

1. dwall>2.0m

2. NHITAC <16 (<10 for SK-I)

3. E_{vis} > 30MeV

The *dwall* is the distance from the ID wall to the primary collision point. The area inside 2 m from the ID tank wall is called the fiducial volume (FV), just like figure 5.3 shows. We apply this reduction becauses the event reconstruction near the wall isn't working well. The event which is happened within the fiducial volume is used for analysis. NHITAC is the cluster of PMTs hit with the highest charge in the OD. E_{vis} is the total energy of the event which assuming that the event generates all Cherenkov rings. The Events that don't satisfy the second condition will be classified as PC events. After these event selections, the event rate will become approximately 8 event / day.

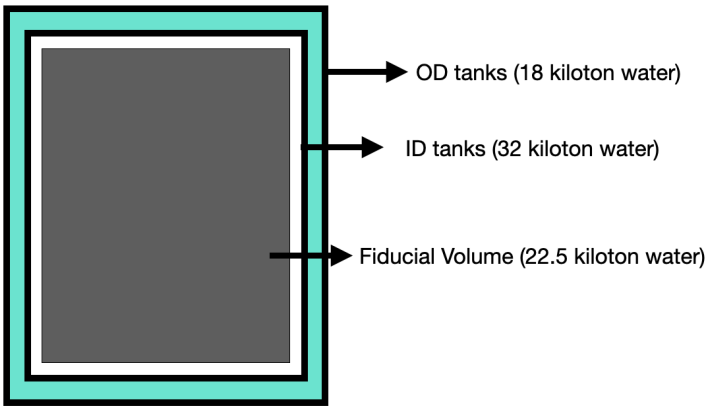

Figure 5.3: Schematic diagram of the OD tank, ID tank and FV of the Super-Kamiokande detector.

Chapter 6

Sensitivity study

6.1 Event Selection

After the FC reduction, an event selection is applied to obtain the final analysis sample.

6.1.1 Event Selection

The target particle we are looking for is neutrino from GUT-monopole-catalyzed proton decay in the sun. Due to oscillations, target particles are $\bar{\nu_e}$ neutrinos and $\bar{\nu_\mu}$ neutrinos, and the energy region is around the energy range of 459 MeV. However, we could see that the dominant neutrino reaction mode of $\bar{\nu_e}$ neutrinos and $\bar{\nu_\mu}$ neutrinos in this energy range is the CCQE. Please see the event reconstruction algorithm chapter and the neutrino reactions chapter.

$$\bar{\nu_e} + p \rightarrow e^+ + n \tag{6.1}$$

$$\bar{\nu_\mu} + p \rightarrow \mu^+ + n. \tag{6.2}$$

Since the leptons produced in the CCQE reaction will be reconstructed in different ways in SK, therefore, the positron and the μ^+ will have extra event reconstruction efficiency and system uncertainty estimates in the final event sample. On the other hand, the neutrino oscillation probability of atmospheric neutrinos, which is the most significant background for this analysis, will also be changed with the energy and zenith angle of the neutrino.

From the first chapter we can see that our target particles are $\bar{\nu_e}$ neutrinos and $\bar{\nu_\mu}$ neutrinos, and from the neutrino reaction chapter, we can see that the CCQE process of anti-neutrinos produces neutrons, and neutrinos produces protons. Note that the protons produced by neutrinos (ν) will interact with other nuclei and release neutrons (via so-called secondary interactions), the CCQE reaction of antineutrinos will also produce many neutrinos through nuclear interactions. However, from the MC simulation result, shown in Figure 6.1 below, we can conclude that the antineutrino CCQE reaction releases more neutrons on average than the neutrino CCQE reaction. Therefore, the neutron is a good parameter that could help us to separate neutrino from antineutrino interactions.

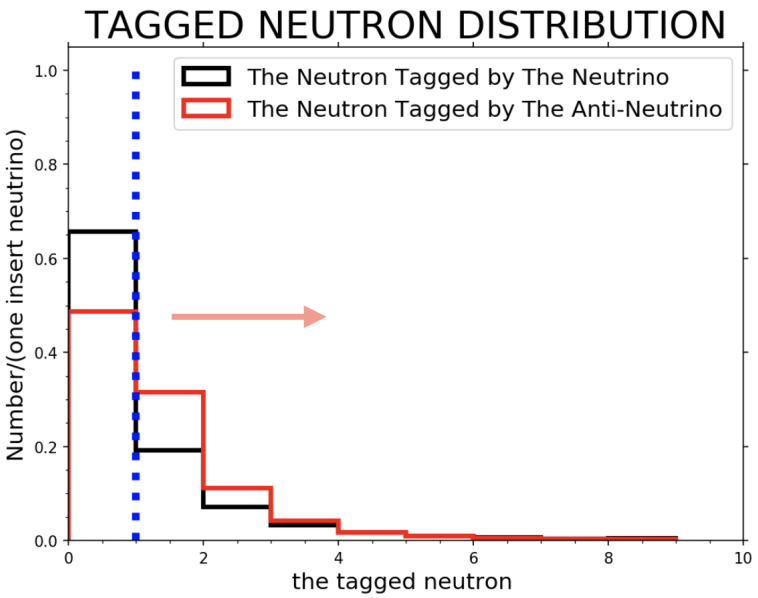

Figure 6.1: Distribution of neutrons in the final state from sub-GeV nuebar and numubar CCQE interactions. Both lines are normalized by area.

Consequently, after we apply all of the reduction of FC, we also need to divide the FC data to different samples by using the number of the Cherenkov rings (one-ring or multi-ring) and the energy of the events, dividing them into more than 1330 MeV(multi-GeV) or not (Sub-GeV). After that, we also separate the Sub-GeV, one ring, samples, which is based on the number of Michel electrons for this sample, neutron number for this sample, and the particle ID (PID). We could conclude from the above table that the dominated reaction mode of the magnetic monopole catalyzed proton decay neutrino is CCQE. And, there is only one lepton that could generate the Cherenkov ring, which equally means there is only a single Cherenkov ring in SK. Therefore, I will focus on the case of SubGeV samples. Details of the event selection for other atmospheric neutrino analyses are present in [70].

The Sub-GeV data will be categorized into 5 sample such as follows :

1. FC sub-GeV single-ring ν_e-like
2. FC sub-GeV single-ring e-like
3. FC sub-GeV single-ring $\bar{\nu_e}$-like
4. FC sub-GeV single-ring ν_μ-like
5. FC sub-GeV single-ring $\bar{\nu_\mu}$-like

The momentum cut for single-ring e-like and mu-like events is different. The single ring e-like events has to satisfy the momentum cut, 100 MeV $>$ $\mathrm{p_e}$ $<$ 1330 MeV, and for μ-like events it is, 200 MeV$<$ $\mathrm{p_\mu}$ $<$ 1330 MeV.

FC sub-GeV single-ring e-like sample contains ν_e CCQE interactions and also could be NC π_0 background events. The e-like sample which the highest fraction of CCQE events is the 0 decay-e sample. For NC π_0 event, one of the two gamma rays produced by π_0 could be missed by reconstruction, therefore the event could be misidentified as a single-ring e-like

event. A specialized π_0 fitter is used to reconstruct the second gamma-ray ring based on the fitted first ring.

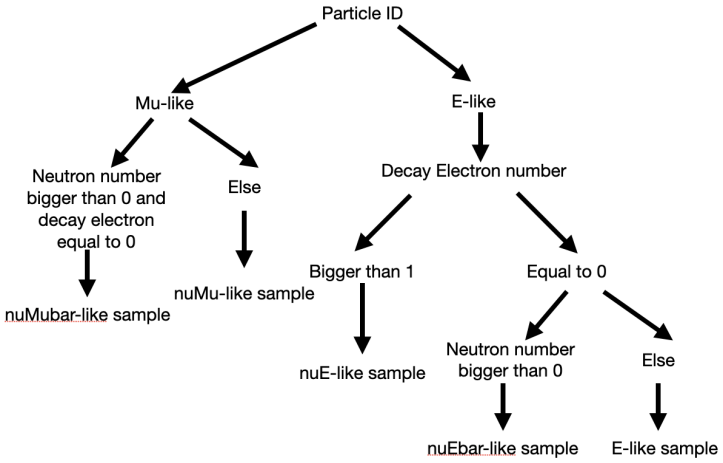

Figure 6.2: schematic diagram about the steps for how to select the FC data to different Sub-GeV samples.

After applying π_0 likelihood method, remaining e-like events are divided into three categories, depending on the detected number of Michel electrons and the neutron number: 0 decay-e sample with no decay electrons with zero tagged neutrons (e-like), 0 decay-e sample with no decay electrons and one or more neutrons ($\bar{\nu_e}$-like), and one decay-e sample which has one or more decay electrons (ν_e-like).

On the other hand, ν_μ CCQE events are expected to produce one decay electron from their muon. FC sub-GeV single-ring μ-like events are divided into two categories according to the number of decay electrons and the number of the neutron: $\bar{\nu_\mu}$-like, ν_μ-like. If the decay electron number is equal to one and the tagged neutron number is more significant than 0, We will select this event to the $\bar{\nu_\mu}$-like the sample. We will choose the remaining events to the ν_μ-like samples.

The other sub-GeV events are π_0-like multi-ring events, which have two or more e-like rings recognized. Figure 5.4 shows the schematic diagram about the steps for selecting the

FC data for different Sub-GeV samples. Table 6.2 and Table 6.3 shows the summary of purities of FC sub-GeV single-ring samples.

Table 6.1: The reaction mode fraction for 459MeV $\bar{\nu_e}$ neutrinos and $\bar{\nu_\mu}$ neutrinos MC, and atmospheric neutrinos MC after event selection.

	$\bar{\nu_e}$	$\bar{\nu_\mu}$	ATM MC
CCQE	80.73%	99.89%	71.24%
CC single π	16.08%	0%	17.80%
CC coherent π	0.322%	0.072%	0.28%
CC multi π production	1.411%	0%	2.076%
NC reaction	1.24%	0.036%	7.854%

Table 6.2: The purities of FC sub-GeV single-ring sample for 459MeV $\bar{\nu_e}$ neutrinos and $\bar{\nu_\mu}$ neutrinos MC, and fraction of total MC

	CC ν_e	CC $\bar{\nu_e}$	CC ν_μ	CC $\bar{\nu_\mu}$	NC event	Fraction
ν_e-like	0%	80.95%	0%	19.04%	0%	0.23%
e-like	0%	99.07%	0%	0.08%	0.84%	27.66%
$\bar{\nu_e}$-like	0%	99.77%	0%	0.05%	0.16%	19.97%
ν_μ-like	0%	1.56%	0%	98.03%	0.39%	28.26%
$\bar{\nu_\mu}$-like	0%	0%	0%	99.75%	0.24%	17.95%

Table 6.3: The purities of FC sub-GeV single-ring sample for atmospheric neutrinos MC

	CC ν_e	CC $\bar{\nu_e}$	CC ν_μ	CC $\bar{\nu_\mu}$	NC event
ν_e-like	79.72%	1.61%	14.21%	2.71%	1.72%
e-like	80.16%	17.18%	1.69%	0.03%	0.90%
$\bar{\nu_e}$-like	59.22%	36.92%	2.69%	0.11%	1.03%
ν_μ-like	1.39%	0.11%	79.84%	17.69%	0.95%
$\bar{\nu_\mu}$-like	0.78%	0%	55.43%	42.96%	0.81%

6.1.2 Sample Binning

The 5 event samples are distributed to more proper bins. The visible energy and reconstructed angle are used to define bins. For angular binning, the cosine value between the direction of the Sun and the reconstructed lepton direction, $\cos(\theta_{Sun})$, is used. This value is

calculated using the sun's position compared to the SK tank at the time of each event. We can check the $\cos(\theta_{sun})$ distribution in Fig. 6.3 that atmospheric neutrino events are almost evenly spread since we could assume that the particle is inserted into the SK isotropically. We cannot use the neutrino direction since it cannot be reconstructed. However, the angular resolution of the lepton angle compared with the neutrino angle is 32 degrees.Therefore, the signal events are not perfectly reconstructed as coming from the direction of the sun and we can could see that the angular distribution for the signal will be more spread. Figures 6.3 shows the angular distributions of the five FC samples for the Signal event and BG event For these samples, 10 equally sized angular bins which span from $\cos(\theta_{sun})$ = -1 to 1 are used.

All samples are further divided into five momentum bins. As a result, events will be distributed in 250 two-dimensional (angle and energy) bins for each Signal and BG respectively. During the fit, the Signal and BG MC bins are merged, so the total number of bins used to fit the flux of monopoles is 250 in total..

Table 6.4: The zenith angle and energy bin in each analysis sample

sample	energy bins	$\cos\theta$ bins
ν_e-like	5 $e^{\pm}$momentum	10 in $[-1, 1]$
e-like	5 $e^{\pm}$momentum	10 in $[-1, 1]$
$\bar{\nu_e}$-like	5 $e^{\pm}$momentum	10 in $[-1, 1]$
ν_μ-like	5 $\mu^{\pm}$momentum	10 in $[-1, 1]$
$\bar{\nu_\mu}$-like	5 $\mu^{\pm}$momentum	10 in $[-1, 1]$

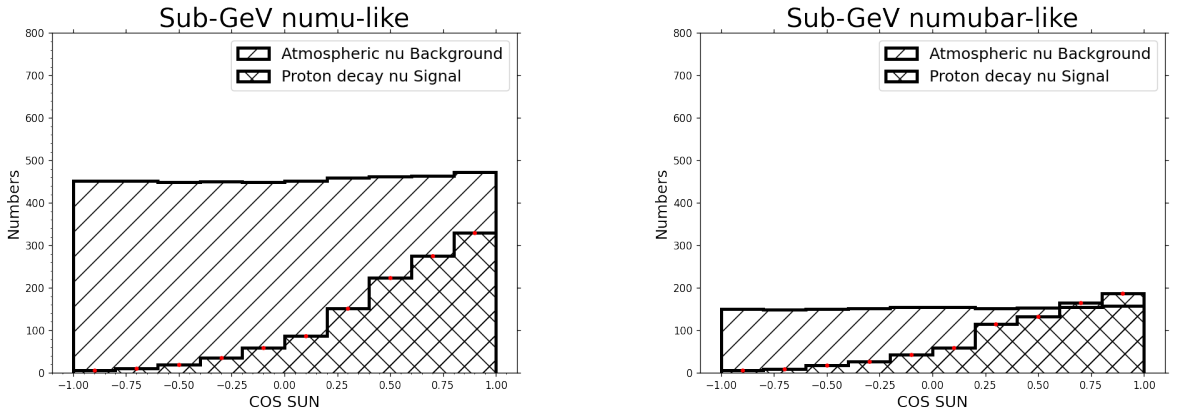

(a)

(b)

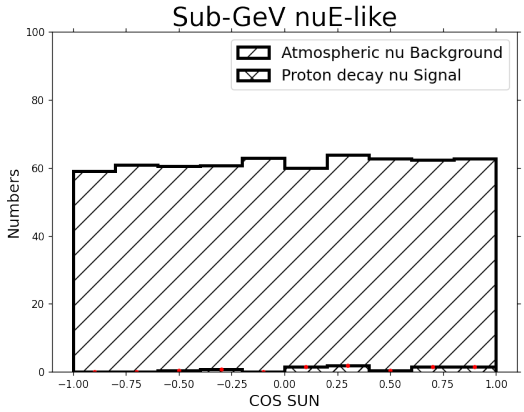

(c)

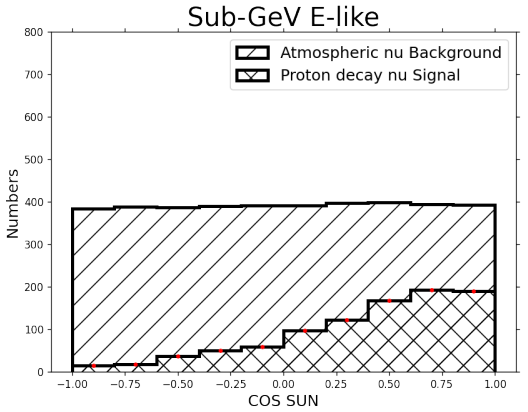

(d)

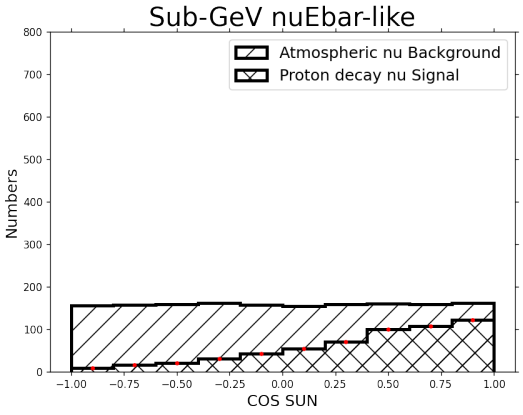

(e)

Figure 6.3: $\cos(\theta_{sun})$ distributions of signal MC and BG atmospheric neutrino.Normalization for the signal is the number of MC events, which is about 20,000 event, related to the Parker Limit. ν_e and ν_μ and background is normalized by the SK-IV livetime, which is 3244 days.

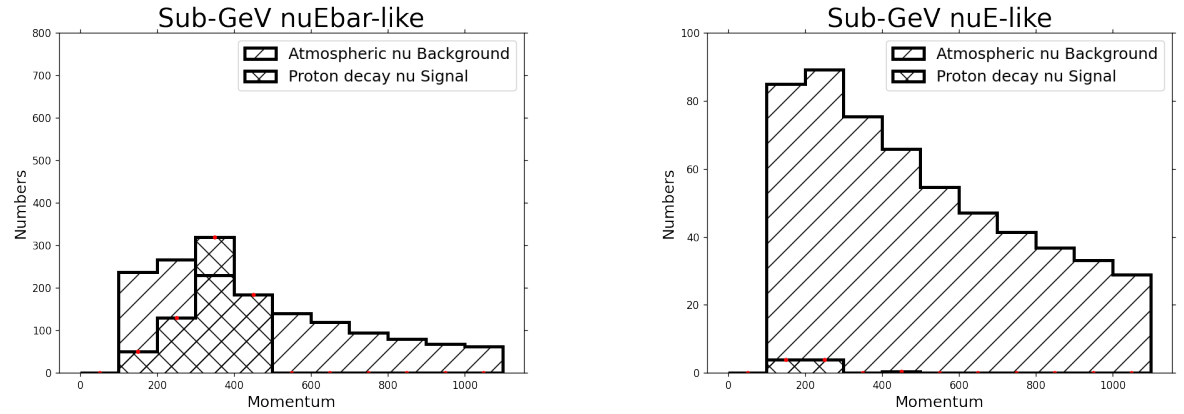

(a)

(b)

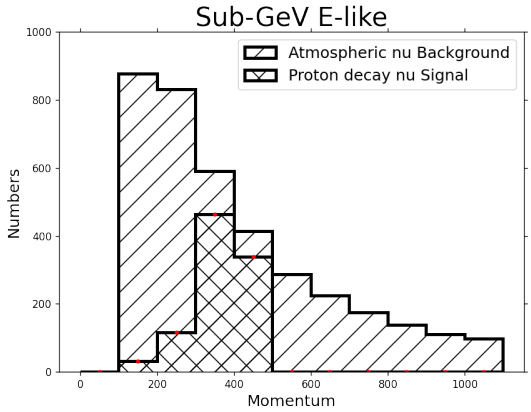

(c)

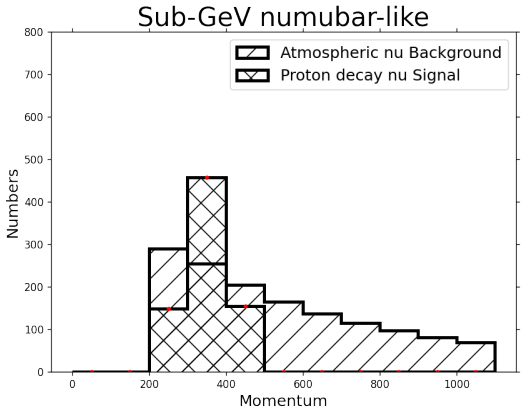

(d)

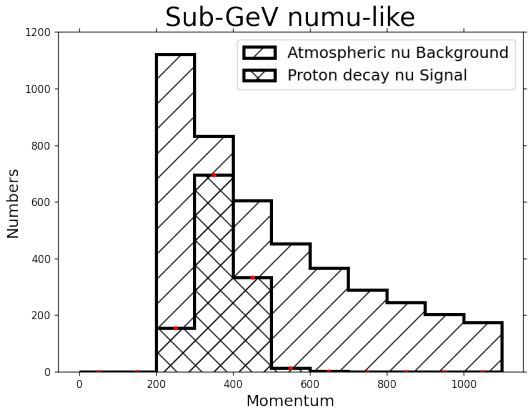

(e)

Figure 6.4: Momentum distributions of signal MC and BG atmospheric neutrino. Normalization for the signal is the number of MC events, which is about 20,000 events, related to the Parker Limit. same as figure 6.3 is normalized by the SK-IV lifetime, which is 3244 days

6.2 Spectral Fit

6.2.1 Fitting Technique

Now, we apply a spectral χ^2 fit to the final momentum and $\cos(\theta_{sun})$ distributions, as shown in the last chapter. By applying the χ^2 spectral fit, we account for the shape difference between the signal and the background distributions.

The χ^2 minimization fit is based on the Poisson distribution. When the data is fitted, it will be fitted with the systematic uncertainties by pull technique [21]. The χ^2 function definition in the analysis is

$$\chi^2 = 2\sum_{i=1}^{\text{nbins}} \left(N_i^{\text{exp}} + N_i^{\text{obs}} \left[\ln \frac{N_i^{\text{obs}}}{N_i^{\text{exp}}} - 1 \right] \right) + \sum_{j=1}^{N_{\text{syserr}}} \left(\frac{\epsilon_j}{\sigma_j} \right)^2, \tag{6.3}$$

$$N_i^{\text{exp}} = \left[N_i^{\text{back}} + \beta \cdot N_i^{\text{sig}} \right] \left(1 + \sum_{j=1}^{N_{\text{syserr}}} f_i^j \frac{\epsilon_j}{\sigma_j} \right) \tag{6.4}$$

where the i is the index of the analysis bin. Here N_i^{exp} is the expectation for bin i, which is generated by the MC (sum of the background and signal). N_i^{sig}, N_i^{back} are the signal MC, background MC event in each bin separately. The N_i^{obs} is the observation data. In data fit, N_i^{obs} should be take as the SK -IV data. The index j is the systematic errors index, while ϵ_j is the fit error parameter, f_i^j is the fractional change of the i-th bin under a 1-sigma variation of the system in the j-th systematic. The 1-sigma error uncertainty is defined as σ_j. The fit is performed using one parameter, β, which denotes signal normalizations. This f_i^j will act separately on the signal and background. After the event selection, the background MC distribution is normalized by the SK-IV lifetime. Since the monopole flux isn't known known, we need to identify the fit point with different β, to determine the sensitivity for detecting the monopole neutrino in SK. The β is zero, means consistent with the no-signal hypothesis. Similarly, β is one related to the monopole neutrino total number is 20,000 at

SK-IV, which is almost related to the Parker Limit, which could calculate by [27]. The χ^2 minimization is carried out for each β in grid according to $\partial\chi^2/\partial\epsilon_j = 0$. We can find further details about the fit technique and the treatment of systematic errors in [70, 16], and is similar to the standard SK oscillation analysis and the indirect dark matter search.

Our analysis is a sensitivity study. Therefore, we use two methods to do the sensitivity study here. The first method is Asimov sensitivity analysis, which uses the nominal background MC assuming 0 signal ($\beta = 0$) as the observation and fits it with and without the systematic error. By comparing the shape of these two curves from the fitting result, we could be quantized how much the systematic errors related to the SK will impact this search. After that, we need to consider that there must be an random statistical differences between the actual data and the MC. Therefore, we will add a random fluctuation to the null hypothesis ($\beta = 0$) MC data and take it as fake data. Then, this simulated data is fitted to test the sensitivity of the SK for magnetic monopole neutrinos. This method is called the toy MC method.

6.2.2 Systematic Errors

The systematic errors in the analysis are calculated through the f_i^j coefficients, as described above. For simplicity, we assumed that the bin content is affected linearly by the error. Therefore, the f_i^j can be defined as a slope of systematic error uncertainty, which is determined by the bin content, which changed by 1 σ. The definition of f_i^j is shown as follows:

$$f_i^j \equiv \frac{\left(N_i^{+\sigma_j} - N_i^{-\sigma_j}\right)}{2N_i^0}. \tag{6.5}$$

The error estimation in our analysis is different with [70]. We take the way that the signal and error bins are split to estimate various errors. That will ensure that signal systematic

is applied to the signal bins and background systematic to the background bins. If the bins should use both errors, it will be applied to both bins. Then the signal bins and background bins will be merged during χ^2 minimization.

The systematics can be divided into signal-specific (S) and background-specific (B). Some systematics errors, such as detector and reconstruction errors, are familiar to signal and background (SB). Since the dominant reaction mode of the signal, the neutrino, is the CCQE, and the atmospheric neutrino could also interact via in CCQE, the CCQE cross-section uncertainty should apply to both signals and background(SB).

The systematic background errors are the neutrino flux, neutrino-interaction cross-section uncertainty. The systematic error of the background, is the same systematic error which was employed in the SK oscillation analysis [70, 16]. Then we select the reconstruction error, and the CCQE cross-section uncertainty and apply them to the signal. In Table 6.1, Table 6.2, Table 6.3, we display the complete list of systematics, the uncertainties, and the fitted pull terms, which is calculated by ϵ_j/σ_j the best-fit point under the toy MC hypothesis, for the signal and background.

Although we use the same systematic error type as the previous SK analysis, because the bin we use here is a two-dimensional bin of momentum and $\cos(\theta_{sun})$, instead of the two-dimensional bin of momentum and zenith angle that previous SK analysis, our f_i^j are different. Our f_i^j distribution here is shown in Figure 6.5

6.2.3 Sensitivity study

To calculate the MC sensitivity, we use atmospheric MC as "fake data." That corresponds to the scenario in which is no evidence shows there is high energy monopole catalyze proton decay is observed in the SK-IV. This hypothesis follows the background distribution, which

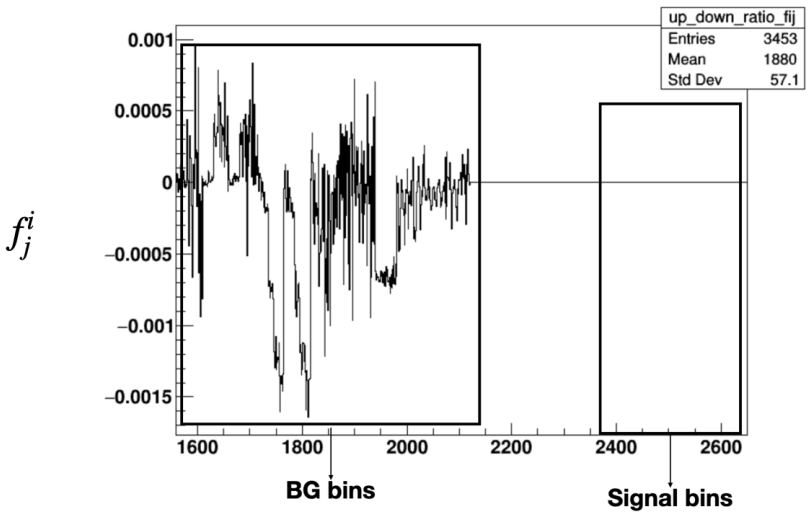
up_down_ratio_fij
Entries 3453
Mean 1880
Std Dev 57.1
0.001
0.0005
0
−0.0005
−0.001
−0.0015
1600
1800
2000
2200
2400
2600
BG bins
Signal bins
f_j^i
Index of analysis bins

(a)

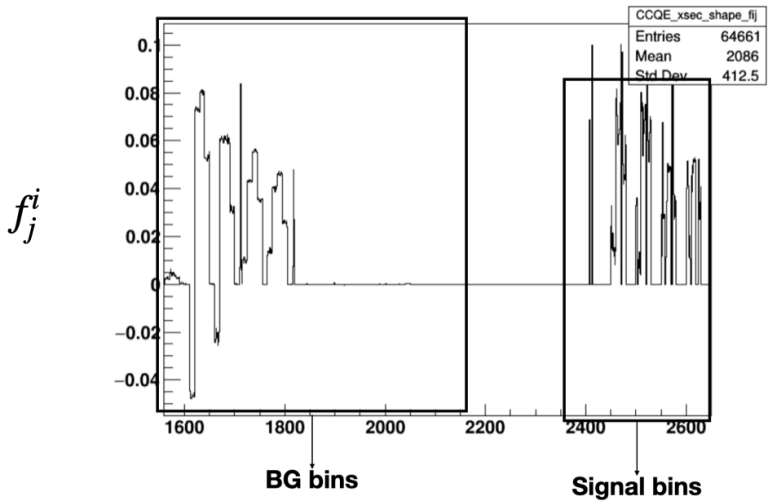
CCQE_xsec_shape_fij
Entries 64661
Mean 2086
Std Dev 412.5
0.1
0.08
0.06
0.04
0.02
0
−0.02
−0.04
1600
1800
2000
2200
2400
2600
BG bins
Signal bins
f_j^i
Index of analysis bins

(b)

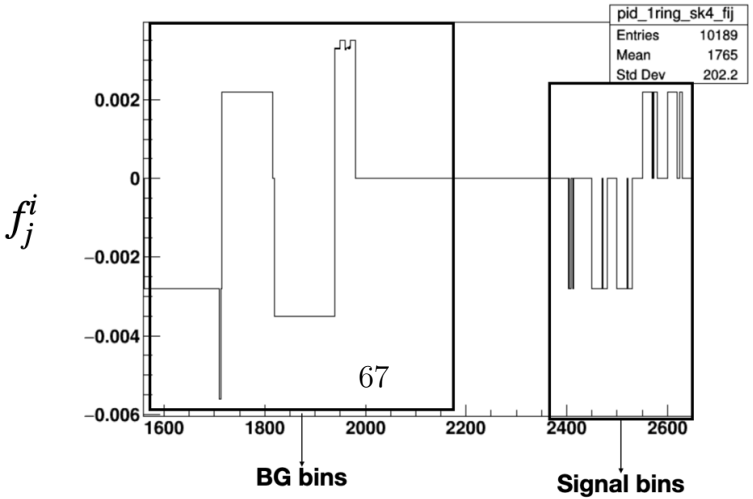
pid_1ring_sk4_fij
Entries 10189
Mean 1765
Std Dev 202.2
0.002
0
−0.002
−0.004
−0.006
1600
1800
2000
2200
2400
2600
BG bins
Signal bins
f_j^i

Table 6.5: Neutrino interaction, particle production, and PMNS oscillation parameter systematic errors for the spectral fits, with 1σ uncertainties and resulting fit pull terms. Errors specific to signal and background are denoted by S and B.

Systematic error	1-σ uncertainty	
CCQE cross section	0.100	SB
DIS model difference	0.100	SB
DIS cross section	0.100	SB
Coherent cross section	1.0	SB
NC CC ratio	0.200	SB
CCQE ν_e $\bar{\nu_e}$ ratio	0.100	SB
CCQE ν_μ ν_e ratio	0.100	SB
CCQE cross section normalization sub GeV	0.100	SB
CCQE cross section normalization multiply GeV	0.100	SB
Hadron simulation	0.100	B
π_0 π ratio	0.400	B
ν $\bar{\nu}$ ratio	0.100	B
θ_{13} error	0.000	B
δm^2_{21} error	1.799	B
θ_{12} error	0.013	B
M_A in CCQE and single meson production	0.100	B
Single meson production cross section	0.100	B
DIS had mult	0.100	B
Q^2 spectrum in DIS (W $< 1.3 GeV/c^2$)	0.100	B
Q^2 spectrum in DIS (W $> 1.3 GeV/c^2$)	0.100	B
DIS normalization in W $> 1.3 GeV/c^2$	0.100	B
Neutron mult	0.100	SB
Neutron multiplicity generator comp	0.100	SB

Table 6.6: SK-IVsystematic errors for the spectral fits, with 1σ uncertainties and resulting fit pull terms. Errors specific to signal and background are denoted by S and B.

Systematic error	1-σ uncertainty	
FC reduction for SK-IV	0.013	SB
FC PC separation for SK-IV	0.000	SB
Ring separation SK-IV	0.100	SB
PID 1ring SK-IV	0.009	SB
PID multi-ring SK-IV	0.100	B
Decay-e tagging SK-IV	0.100	SB
Fiducial volume SK-IV	0.019	SB
π decay tagging error	0.100	B
Up stop through separation SK-IV	0.006	B
Up stop energy cut SK-IV	0.017	B
Up/down asymmetry energy calibration SK-IV	0.004	B
Non Showering BG sub SK-IV	0.079	B
Non ν_e BG Multi-ring elike SK-IV	0.115	B
Non ν_e BG 1ring elike SK-IV	0.175	SB
Non ν_e BG elike SK-IV	0.009	SB
Non ν bg μ like	0.009	SB
Sub-GeV 2-ring π_0 SK-IV	0.056	B
Energy calibration	2.3	SB

Table 6.7: Flux Systematic errors that are independent in for the spectral fits, with 1σ uncertainties and resulting fit pull terms. Errors specific to signal and background are denoted by S and B.

Systematic error	1-σ uncertainty	
Solar Activity SK-IV	0.070	B
Absolute Normalization E less1GeV	0.25	B
ν $\bar{\nu}$ ratio E less 1GeV	0.019	B
ν $\bar{\nu}$ ratio E bigger 10GeV	0.050	B
ν_e $\bar{\nu_e}$ E less 1GeV	0.050	B
ν_e $\bar{\nu_e}$ E bigger 10GeV	0.079	B
ν_μ $\bar{\nu_\mu}$ E less 1GeV	0.019	B
ν_μ $\bar{\nu_\mu}$ E bigger 10GeV	0.150	B
Up Down ratio	0.009	B
Horizontal Vertical ratio	0.009	B
K π ratio	0.100	B
Neutrino path length	0.100	B
Absolute Normalization E bigger 1GeV	0.150	B
Relative Normalization FC multi-GeV	0.050	B
ν $\bar{\nu}$ ratio 1 E bigger 10GeV	0.029	B
ν_μ $\bar{\nu_\mu}$ 1 E bigger 10GeV	0.050	B
ν_μ $\bar{\nu_\mu}$ 1 E bigger 10GeV	0.059	B
Matter Effect Error	0.068	B

means the signal's normalization is $\beta = 0$, and the background normalized to the SK-period's lifetime. We determine the confidence of the monopole neutrino signal by calculating the difference of chi-square to the best fit chi-square when the signal normalizations parameter is changing:

$$\chi^2 \leq \chi^2_{\rm min} + \Delta\chi^2. \tag{6.6}$$

This analysis has only one parameter and we set the confidence level to 90% for the convenience of comparison with other studies. Table 6.8 shows the $\Delta\chi^2$ values we use for drawing confidence regions. As an example of the χ^2 contour output, we display the Asimov sensi-

Table 6.8: Values of $\Delta\chi^2$ corresponding to confidence levels used in this thesis..

1-α (%)	m = 1
68.27	1.00
90.	2.71
95.	3.84

tivity fit results in Figure 6.6. In all such χ^2 contour plots, the black lines correspond to 90% confidence level (CL) intervals, the blue lines correspond to the fit result, which does not use the systematic error for fitting, and the red lines correspond to the fit result which uses the systematic error for fitting.

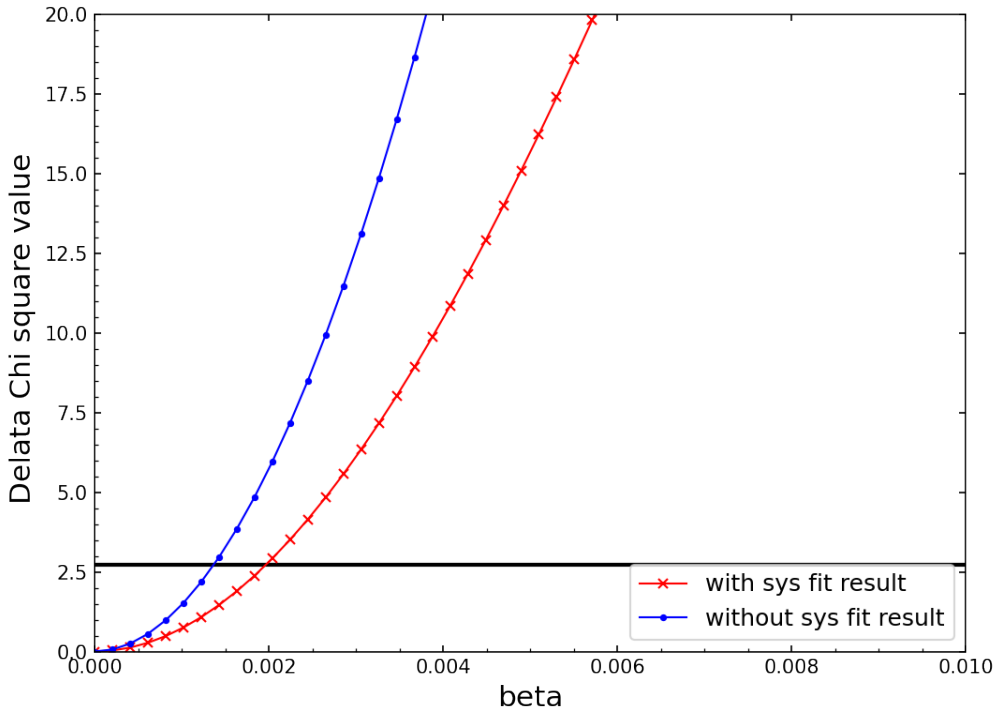

Figure 6.6: The Asimov sensitivity analysis fit for 459MeV Monopole neutrino by assuming the true point is at null hypothesis.

According to Figure 6.6, we can get that the normalization at 90% C.L. is 0.00203 which is correspond to 40.6 monopole events. The number of $\bar{\nu_e}$ event is 18.08 and the number of $\bar{\nu_\mu}$ event is 22.51. To estimate how much the systematic error will impact our experiment, we assume that the "true point" of the next Asimov fit is set as the normalization at 90% CL obtained from Figure 6.6 . The result is shown shown in Figure 6.7.

We can see that if we set the reference point at beta equal to 0.00204, then the χ^2 with a systematic error when no magnetic monopole neutrino ($\beta = 0$) is 3.58, and the χ^2 without systematic error is 7.35, respectively. Although the systematic error impacts the sensitivity of our analysis, the χ^2 at $\beta = 0$ is still higher than the 90% confidence level χ^2, which is 2.71. That shows that could cause magnetic monopole neutrinos in SK with at slightly better than

90% CL.

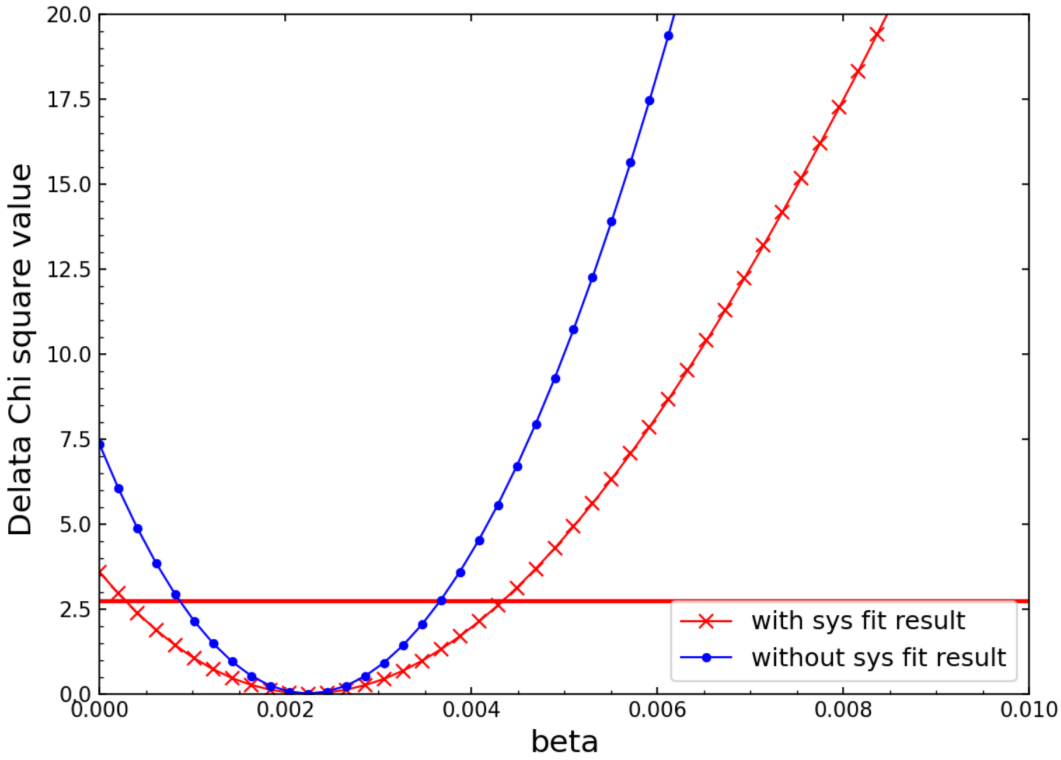

Figure 6.7: The Asimov sensitivity analysis fit for 459MeV Monopole neutrino by assuming the "true point" of the fitting is normalization at 90% C.L. from Fig 6.6

We have seen that although the impact of systematic errors is not very large, it still affects our final results. Therefore, I investigated the source of systematic errors. The investigation method is as follows:

Initially, removed the 77 systematic error terms one by one, assuming that these recurring error terms should be zero, and then perform the Asimov sensitivity test. If this systematic error is vast for our fitting, then the number of magnetic monopole neutrinos with a 90% confidence level will reduce if this error is deleted. If the influence of this systematic error is not particularly large, then even if this periodic error is deleted, we will find that the number of neutrinos in the magnetic monopole has not decreased too much. Our fitting curve will coincide with the error-free Asimov sensitivity analysis when we delete all the

systematic errors.

Although we have 77 systematic errors here, we can classify various systematic errors. For example, we can set the flux error to the same type of systematic error because this systematic error will only affect the background in our analysis, atmospheric neutrinos.

The final fitting result is shown in Figure 6.8 below. We can see that the primary error term comes from six sources. That is single meson production cross-section, M_A in CCQE and Single Meson Production, neutron tagging, atmospheric neutrinos flux, Nuclear Effect in ^{16}O Nucleus, CCQE cross section. The impact of these errors on the analysis is listed in the table below.

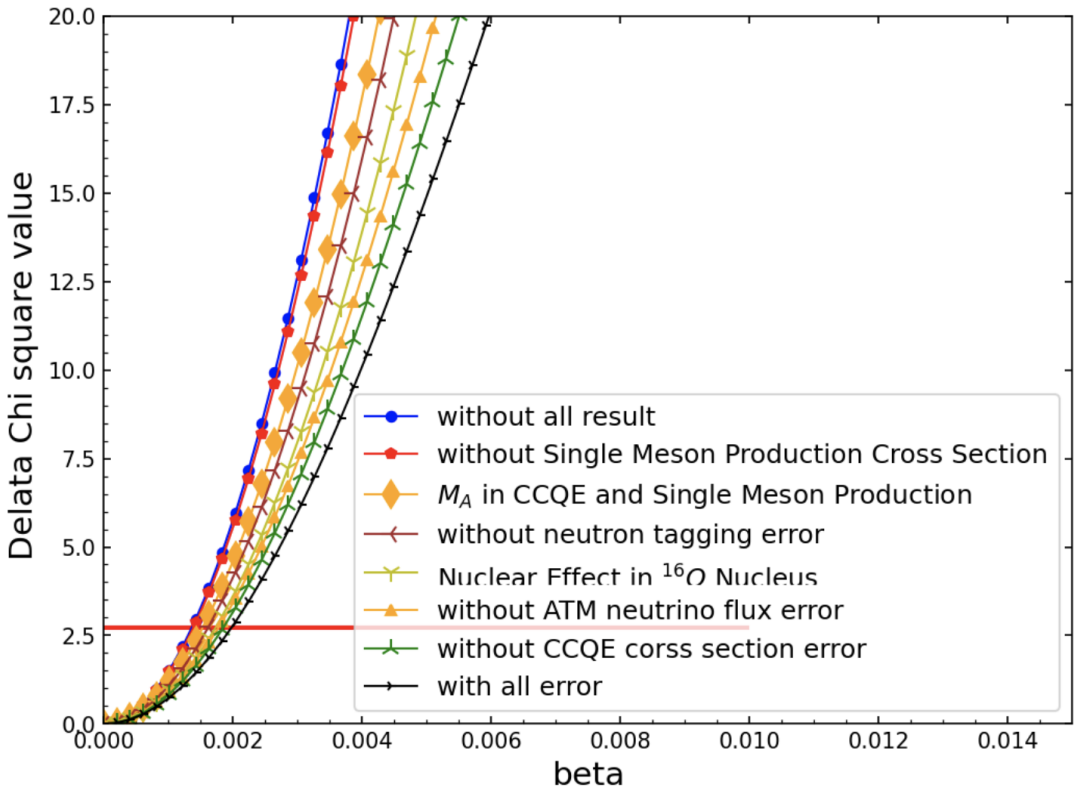

Figure 6.8: The Asimov sensitivity analysis fit for 459MeV Monopole neutrino by using different systematics error

Table 6.9: The value of β at the 90% C.L. changes for each of mainly contribute errors.

β	the error which is omitted
0.00204	no error is rejected
0.00185	CCQE cross section
0.00177	Atmospheric Neutrinos Flux
0.00172	Nuclear Effect in ^{16}O Nucleus
0.00161	Neutron Tagging
0.00152	M_A in CCQE and Single Meson Production
0.00138	Single Meson Production Cross Section

Single Meson Production Cross Section Uncertainty in the cross-section of single meson production is estimated to be 20% by investigating the difference between the expectation and experimental data of $\nu_\mu p \to \mu^- p\pi^+$ observation. $\nu_\mu n \to \mu^- p\pi^0$ interaction is less understood as there are only few experiment results. Hence the additional uncertainty is estimated by comparison with the Hernandez model. The cross-section ratio of $\nu_\mu n \to \mu^- p\pi^0$ is shown in the dashed line in figure 6.9. It is considered that π^0 production interaction has 40% uncertainty relative to the $\pi^\pm$ emitting interactions.

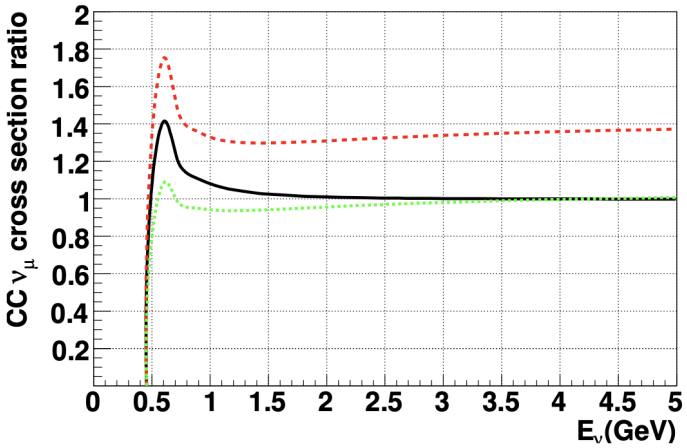

Figure 6.9: Predicted cross section of the Hernandez model normalized by that of the Rein and Sehgal model for $\nu_\mu p \to \mu^- p\pi^+$ (solid line), $\nu_\mu n \to \mu^- p\pi^0$ (dashed line) and $\nu_\mu n \to \mu^- n\pi^+$ (dotted line).[53]

CCQE Cross Section The cross-section CCQE for bound nucleon is calculated based on the Smith and Monitz Fermi-gas model. The difference from the Nieves model is set to as the 1σuncertainty for CCQE cross-section [50]. Figure 6.10 shows the calculated CCQE cross-section ratio of the Nieves model to Smith and Monitz model as a function of neutrino energy for the total cross-section.

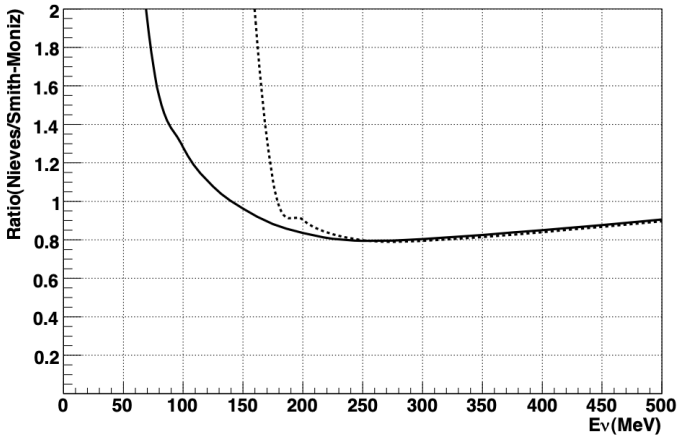

Figure 6.10: Ratio of CCQE cross section, Nieves model normalized by the Smith and Monitz model. [53]

Nuclear Effect in ^{16}O Nucleus The cross-section of pion final state interactions inside nuclei is compared between NEUT simulation and external experimental data. The cross-sections of these last state interactions in the simulation are varied with the weighing method so that the difference with the experimental data is 1σ as shown in figure 6.11. Then the difference between the minimum and maximum weights on each simulated event is then used to compute the uncertainty on the nuclear effect in the oxygen nucleus.

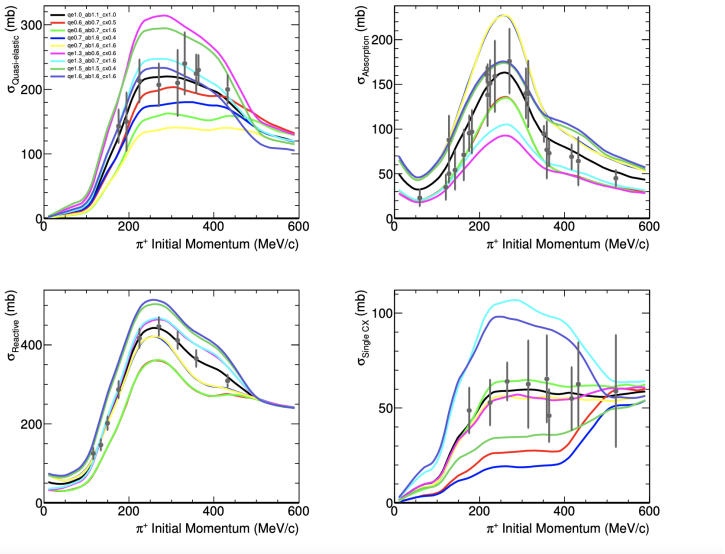

Figure 6.11: π^+ scattering on carbon target in: quasi-elastic channel (top left), absorption channel (top right), total reaction channel (bottom left) and single charge exchange channel (bottom right).[53]

M_A in CCQE and Single Meson Production For M_A in CCQE and single meson production, the difference of Q^2 spectrum between $M_A = 1.2$ and $M_A = 1.1$ is set to be the systematic uncertainty to take into account the 10% uncertainty of M_A parameter.

Neutron Tagging The uncertainty in Neutron Tagging is estimated by comparing the data and MC difference which is studied by R. Akutsu's Ph.D. thesis by using neutrons produced in CC ν_μ interactions in the T2K beam, and the MC generators NEUT 5.4.0 and GENIE.

These six error sources can be expected to be reduced in the future. For meson exchange current, the sources of these errors are mainly from the meson and nucleon reactions used in Monte Carlo simulation. These systematic errors may be reduced in the future when we use multiple models for Monte Carlo simulation.

The error for neutron tagging is mainly due to the low efficiency of neutron tagging in

SK. However, we can expect that this error will be significantly decreased when gadolinium is put into SK in the future. Gadolinium has a very high neutron capture cross-section, so it will improve the efficiency of the neutron tagging in SK.

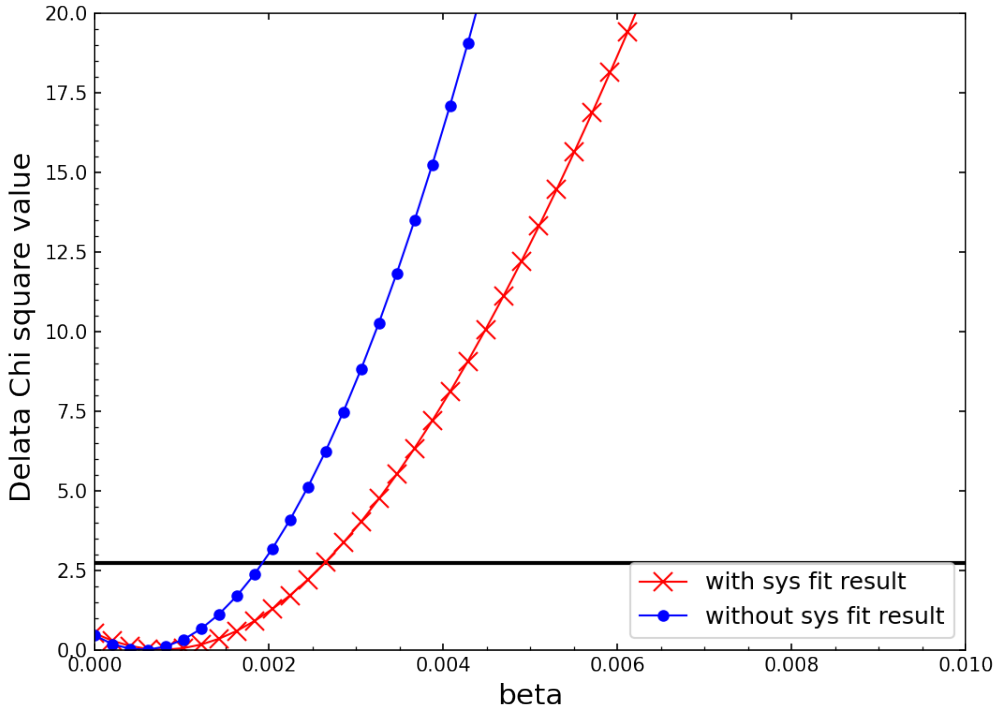

Figure 6.12: The toy MC sensitivity analysis fit for 459MeV Monopole neutrino by assuming the true point is at null hypothesis.

It may be more challenging to reduce the error caused by the reaction cross-section, nucleon axial mass, and the atmospheric neutrino flux because if we want to reduce the systematic error of these items, new models and new experimental data are required at the same time. The experimental data has not been updated recently. So these systematic errors are more difficult to improve.

After we use the Asimov sensitivity test to estimate the systematic error effect of our sensitivity study, we use the toy MC method to evaluate the flux of the magnetic monopole

neutrino in SK. We display the toy MC sensitivity fit results in Figure 6.9. We find that the minimum χ^2 has risen a lot compared to the Asimov sensitivity test. That is because we added random fluctuations to the null hypothesis MC when doing the toy Monte Carlo sensitivity test. As we state before, we are more concerned about is the difference of χ^2 with the change of the normalization, as shown in Figure 6.12.

According to Figure 6.12, we can get that the normalization at 90% C.L. is 0.00265 which is correspond to 51 monopole events. The number of $\bar{\nu_e}$ event is 22.71 and number of $\bar{\nu_\mu}$ event is 28.28.

Assuming that the total flux of the magnetic monopole neutrinos is I_0, the total number of events N_{total} is as follows:

$$N_{\text{total}} = N_{\text{target}}\, T\epsilon_{\text{det}}\,(T) I_0 \sigma. \tag{6.7}$$

Here, $\epsilon_{\text{det}}\,(T)$ represents the detection efficiency which depends over the run time T, and N_{target} represents the total number of water molecule contained in the SK fiducial volume, which is 22.5 kilotons water. Here T integrates over the entire lifetime, the entire SK-IV period is 3224 days. By setting N_{total} equal to Asimov sensitivity study result, the normalization at 90% C.L. is 0.00203 which is correspond to 40.6 monopole events, with number of $\bar{\nu_e}$ event is 18.08 and the number of $\bar{\nu_\mu}$ event is 22.5. The reaction cross-section(σ) of a neutrino will change with different neutrino types and neutrino energy, but all signal neutrinos in this analysis have single energy of 459MeV, so we don't need to consider the influence of neutrino energy on the neutrino interacted cross-section. For the 459MeV anti-electron neutrino and anti-muon neutrino, their reaction cross sections per nucleon are calculated by NEUT, which is :

$$\sigma_{\bar{\nu_e}} = 2.145 \times 10^{-38}\ \text{cm}^{-2}, \sigma_{\bar{\nu_\mu}} = 1.956 \times 10^{-38}\ \text{cm}^{-2}. \tag{6.8}$$

And the detection efficiency here assumes as 1. The total flux of the magnetic monopole neutrinos on Earth is found as follows:

$$I_0 < 9.49 \text{ cm}^{-2} \text{ s}^{-1} (90\% \text{ C.L. }). \tag{6.9}$$

The magnetic monopole neutrinos emission rate and flux on Earth have a relationship like this [35]:

$$I_0 \simeq \frac{1}{4\pi R^2} \frac{BR_{p\to\bar{\nu}}}{m_p c^2} \frac{d\epsilon}{dt}. \tag{6.10}$$

where $BR_{p\to\bar{\nu}}$ is the direct proton decay branching ratio. Here R is the average Earth-Sun distance. We use the distance between earth and sun as 1.496×10^8 km. The $\frac{d\epsilon}{dt}$ is the magnetic monopole neutrinos emission rate. m_p is the mass of proton. Then the magnetic monopole neutrinos emission rate is calculate as follows:

$$\frac{d\epsilon}{dt} \left(\frac{BR_{p\to\bar{\nu}}}{10^{-4}} \right) < 2.24 \times 10^{27} \text{ s}^{-1} (90\% \text{ C.L. }). \tag{6.11}$$

This could also calculate the magnetic monopole neutrinos emission rate:

$$f_p = \int n_M \sigma_R v_{rel} \rho_H N_A d^3x = N_M \sigma_R v_{rel} \rho_H N_A \text{ decay /s}. \tag{6.12}$$

Here, n_M is the number density of magnetic monopoles in the sun, and N_M is the abundance of magnetic monopoles in the entire solar core. σ_R is the cross-section of the Rubakov effect and in order to facilitate the comparison with the previous SK results, we use 1mb. And $v_{rel}$is the relative velocity of the magnetic monopole and the proton, which is taken as $v_{rel} = \beta_{rel} \text{c} \, (= 2 \times 10^{-3} \text{c})$[68]. $\rho_H \, (= 50.4 \text{ g/cm}^3)$ is the mass density of hydrogen at the center of the sun. N_A is Avogadro's number. When we doing the caculation, we used the approximation function, which is the function on the right.

Therefore, the abundance of magnetic monopoles in the entire solar core could be calculated as:

$$N_M \left(\frac{\sigma_R}{1\text{mb}}\right) \left(\frac{BR_{p\to\bar{\nu}}}{10^{-4}}\right) < 4.01 \times 10^{15} (90\%\ \text{C.L. }). \tag{6.13}$$

The relationship between this number and the magnetic monopole flux in the universe is as follows $N_M = 10^{41} F_M$, where F_M is the astrophysical monopole abundance, as introduced in Chapter 4. Consequently, after we estimate the flux of the magnetic monopole neutrino in SK, according to Figure 6.6. We could calculate that the astrophysical monopole abundance in the universe is

$$F_M \left(\frac{\sigma_R}{1\text{mb}}\right) \left(\frac{BR_{p\to\bar{\nu}}}{10^{-4}}\right) < 4.01 \times 10^{-26}\ \text{cm}^{-2}\ \text{s}^{-1}\text{sr}^{-1} (90\%\ \text{C.L. }). \tag{6.14}$$

To visualize the analysis results, we have shown the 90% (CL) allowed signal multiplied by 50, obtained from the Asimov sensitivity study, with all event sample spectra overlaid for atmospheric neutrino MC.

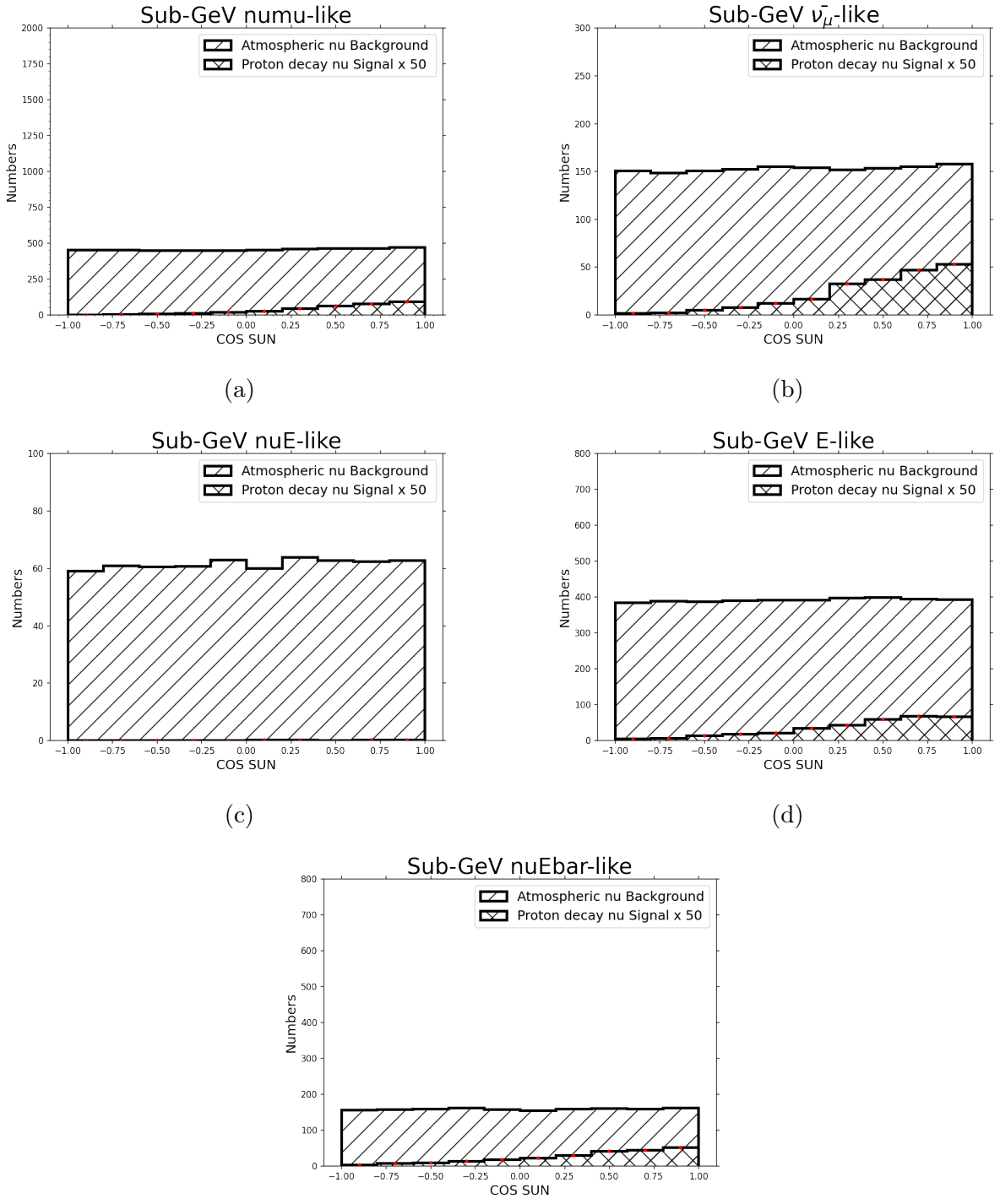

Figure 6.13: $\cos(\theta_{sun})$ distributions The background is normalized by the SK-IV lifetime, which is 3244 days

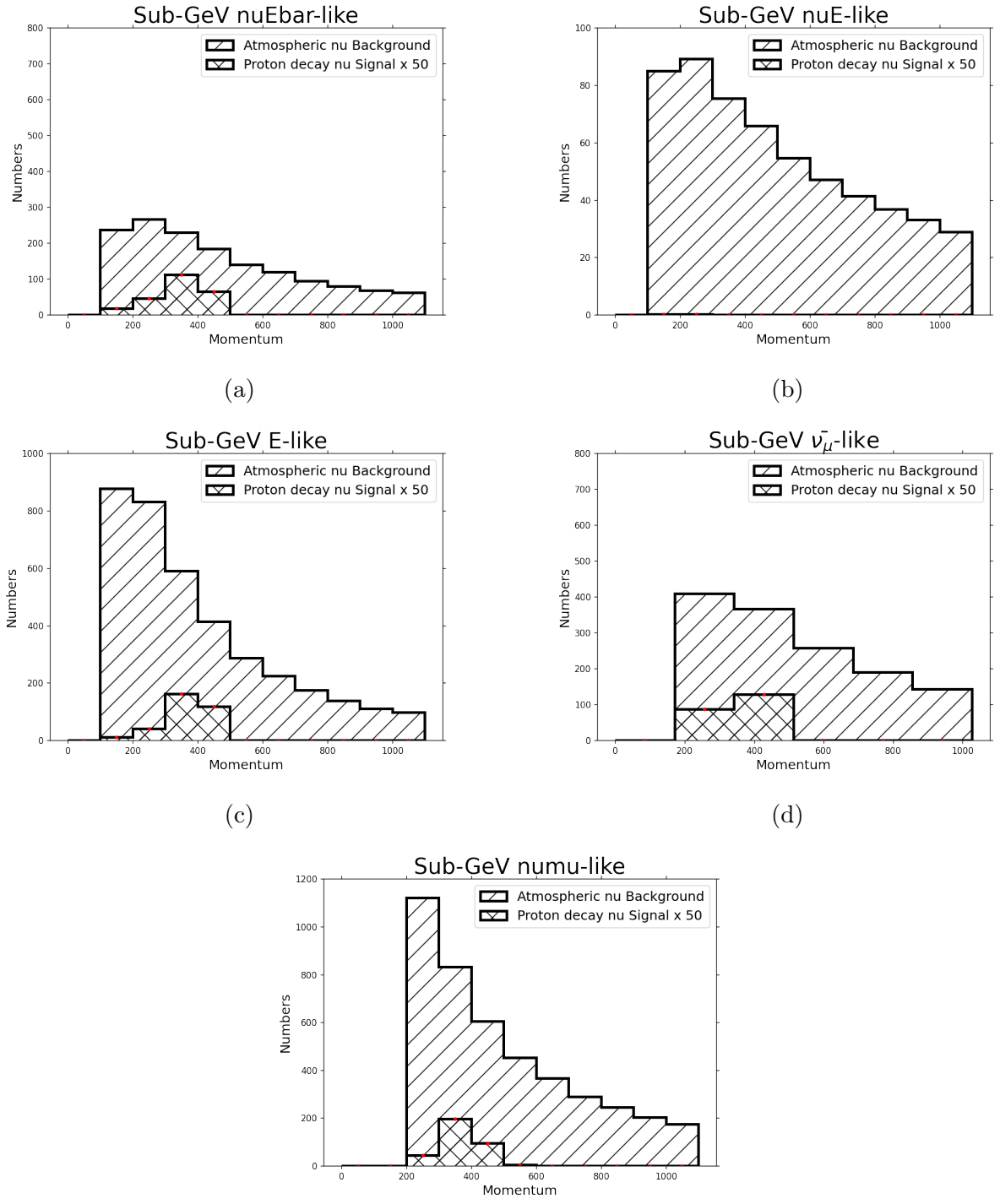

Figure 6.14: Momentum distributions from the Asimov sensitivity study. The background is normalized by the SK-IV lifetime, which is 3244 days

Chapter 7

Summary and Future Prospects

Here is the sensitivity study result of SK to detect magnetic monopole neutrinos.

$$F_M \left(\frac{\sigma_0}{1\text{mb}}\right)\left(\frac{BR_{p\to\bar{\nu}}}{10^{-4}}\right) < 4.01\times10^{-26}\ \text{cm}^{-2}\ \text{s}^{-1}\text{sr}^{-1}(90\%\ \text{C.L.}\ ) \tag{7.1}$$

Compared with the previous results of SK [68],

$$F_{\text{M}} \left(\frac{\sigma_0}{1\text{mb}}\right)\left(\frac{f_{\pi^+}}{0.5}\right) < 6.3\times10^{-24}\left(\frac{\beta_{\text{M}}}{10^{-3}}\right)^2\ \text{cm}^{-2}\ \text{s}^{-1}\text{sr}^{-1}(90\%\ \text{C.L.}\ ) \tag{7.2}$$

we can see that if we search the monopole catalyze proton decay by using the direct mode, the SK will be roughly two orders of magnitude more sensitive than when searching for the indirect proton decay.

However, these results still need further discussion. For example, as we mentioned before, we may need to consider the co-annihilation of magnetic monopoles in the Sun. Nevertheless, we also need to consider the dependence of the Rybakov effect cross-section with the speed of the magnetic monopole. In this analysis, we only take the cross-section of the Rybakov effect as a fixed value, which is about one milibarn.

More importantly, we can see that our result has the same shape as a result obtained by indirect proton decay. It is the product of the flux of the magnetic monopole in the universe and the branching ratio of the corresponding proton decay. So far, we have not been able to confirm the existence of proton decay after various experiments, so the branching ratio of proton decay is still uncertain in our analysis.

However, the result of our sensitivity analysis still brought us an exciting result. And we will use the result to fit the SK-IV data to test whether the magnetic monopole neutrino exists.

SK is now running as a new phase, SK-Gd, which dissolves Gadolinium (Gd) in the tank. Gd has a large capture cross-section of neutrons. Therefore, the neutron tagging technology has improved. This phase started in August 2020, and the atmospheric neutrino events, which is the background of our analysis, are expected to decrease. That could contribute to the better sensitivity of proton decay searches. In addition, the Hyper-Kamiokande project (HK) [54], the successor to SK, has started its construction and plans to operate in 2027. The magnitude is planned to be ten times larger than SK. It will be a cylindrical water tank of 74 m diameter and 60 m height, and will use 40,000 PMTs and 260 kilotons of pure water. HK is expected to contribute to our analysis with more high statistics.

Bibliography

[1] M. Aartsen, R. Abbasi, M. Ackermann, J. Adams, J. Aguilar, M. Ahlers, D. Altmann, C. Arguelles, T. Arlen, J. Auffenberg, et al. Search for non-relativistic magnetic monopoles with icecube. *The European Physical Journal C*, 74(7):1–19, 2014.

[2] K. Abe, L. Ahrens, K. Amako, S. Aronson, E. Beier, J. Callas, P. Connolly, D. Cutts, D. Doughty, L. Durkin, et al. Precise determination of sin 2 θ w from measurements of the differential cross sections for ν p $\mu\rightarrow$ ν p μ and ν^- p $\mu\rightarrow$ ν^- p μ. *Physical review letters*, 56(11):1107, 1986.

[3] K. Abe, C. Bronner, G. Pronost, Y. Hayato, M. Ikeda, K. Iyogi, J. Kameda, Y. Kato, Y. Kishimoto, L. Marti, et al. Search for nucleon decay into charged antilepton plus meson in 0.316 megaton· years exposure of the super-kamiokande water cherenkov detector. *Physical Review D*, 96(1):012003, 2017.

[4] K. Abe, Y. Hayato, T. Iida, K. Iyogi, J. Kameda, Y. Kishimoto, Y. Koshio, L. Marti, M. Miura, S. Moriyama, et al. Calibration of the super-kamiokande detector. *Nuclear Instruments and Methods in Physics Research Section A: Accelerators, Spectrometers, Detectors and Associated Equipment*, 737:253–272, 2014.

[5] A. Abulencia, D. Acosta, J. Adelman, T. Affolder, T. Akimoto, M. Albrow, D. Ambrose, S. Amerio, D. Amidei, A. Anastassov, et al. Direct search for dirac magnetic monopoles in p p collisions at s= 1.96 tev. *Physical review letters*, 96(20):201801, 2006.

[6] S. K. Agarwalla, Y. Kao, and T. Takeuchi. Analytical approximation of the neutrino oscillation matter effects at large θ 13. *Journal of High Energy Physics*, 2014(4):1–42, 2014.

[7] C. H. Albright, C. Quigg, R. Shrock, and J. Smith. Neutrino-proton elastic scattering: Implications for weak-interaction models. *Physical Review D*, 14(7):1780, 1976.

[8] J. Arafune and M. Fukugita. A limit on the solar monopole abundance. *Physics Letters B*, 133(6):380–384, 1983.

[9] Y. Ashie, J. Hosaka, K. Ishihara, Y. Itow, J. Kameda, Y. Koshio, A. Minamino, C. Mitsuda, M. Miura, S. Moriyama, et al. Measurement of atmospheric neutrino oscillation parameters by super-kamiokande i. *Physical Review D*, 71(11):112005, 2005.

[10] D. Bakari, S. Cecchini, H. Dekhissi, J. Derkaoui, G. Giacomelli, M. Giorgini, G. Mandrioli, A. Margiotta, M. Ouchrif, L. Patrizii, et al. Magnetic monopoles, nuclearites, q-balls: a qualitative picture. *arXiv preprint hep-ex/0004019*, 2000.

[11] G. Barr, T. Gaisser, P. Lipari, S. Robbins, and T. Stanev. Three-dimensional calculation of atmospheric neutrinos. *Physical Review D*, 70(2):023006, 2004.

[12] G. Battistoni, A. Ferrari, T. Montaruli, and P. Sala. The fluka atmospheric neutrino flux calculation. *Astroparticle Physics*, 19(2):269–290, 2003.

[13] R. Beck and R. Wielebinski. Magnetic fields in the milky way and in galaxies (revised version of march 2021). *arXiv preprint arXiv:1302.5663*, 2013.

[14] R. Becker-Szendy, R. M. Bionta, C. Bratton, D. Casper, R. Claus, B. Cortez, S. Dye, S. Errede, G. Foster, W. Gajewski, et al. Imb-3: A large water cherenkov detector for nucleon decay and neutrino interactions. *Nuclear Instruments and Methods in Physics Research Section A: Accelerators, Spectrometers, Detectors and Associated Equipment*, 324(1-2):363–382, 1993.

[15] B. Cabrera. First results from a superconductive detector for moving magnetic monopoles. *Physical Review Letters*, 48(20):1378, 1982.

[16] K. Choi, K. Abe, Y. Haga, Y. Hayato, K. Iyogi, J. Kameda, Y. Kishimoto, M. Miura, S. Moriyama, M. Nakahata, et al. Search for neutrinos from annihilation of captured low-mass dark matter particles in the sun by super-kamiokande. *Physical review letters*, 114(14):141301, 2015.

[17] E. R. Davies. *Machine vision: theory, algorithms, practicalities*. Elsevier, 2004.

[18] M. Derrick, P. Gregory, L. Hyman, K. Jaeger, D. Lissauer, R. Miller, B. Musgrave, J. Phelan, P. Schreiner, R. Singer, et al. Properties of the hadronic system resulting from ν^- μ p interactions. *Physical Review D*, 17(1):1, 1978.

[19] P. A. M. Dirac. Quantised singularities in the electromagnetic field. *Proceedings of the Royal Society of London. Series A, Containing Papers of a Mathematical and Physical Character*, 133(821):60–72, 1931.

[20] A. Drukier and S. Nussinov. Monopole pair creation in energetic collisions: is it possible? *Physical Review Letters*, 49(2):102, 1982.

[21] G. Fogli, E. Lisi, A. Marrone, D. Montanino, and A. Palazzo. Getting the most from the statistical analysis of solar neutrino oscillations. *Physical Review D*, 66(5):053010, 2002.

[22] J. A. Frieman, K. Freese, and M. S. Turner. Superheavy magnetic monopoles and main-sequence stars. *The Astrophysical Journal*, 335:844–861, 1988.

[23] R. Gardner, B. Cabrera, M. Huber, and M. Taber. Search for cosmic-ray magnetic monopoles using a three-loop superconductive detector. *Physical Review D*, 44(3):622, 1991.

[24] G. Giacomelli, M. Giorgini, T. Lari, M. Ouchrif, L. Patrizii, V. Popa, P. Spada, and V. Togo. Magnetic monopole bibliography. *arXiv preprint hep-ex/0005041*, 2000.

[25] G. Giacomelli and M. Sioli. Astroparticle physics. *arXiv preprint hep-ex/0211035*, 2002.

[26] M. Glück, E. Reya, and C. Sieg. Spin-dependent structure functions of real and virtual photons. *The European Physical Journal C-Particles and Fields*, 20(2):271–281, 2001.

[27] D. E. Groom. In search of the supermassive magnetic monopole. *Physics Reports*, 140(6):323–373, 1986.

[28] S. W. Hawking and I. L. Moss. Supercooled phase transitions in the very early universe. *Physics Letters B*, 110(1):35–38, 1982.

[29] Y. Hayato. Neut. *Nuclear physics. B, Proceedings, supplements*, 112(1-3):171–176, 2002.

[30] M. Honda, T. Kajita, K. Kasahara, and S. Midorikawa. Comparison of 3-dimensional and 1-dimensional schemes in the calculation of atmospheric neutrinos. *Physical Review D*, 64(5):053011, 2001.

[31] M. Honda, T. Kajita, K. Kasahara, and S. Midorikawa. New calculation of the atmospheric neutrino flux in a three-dimensional scheme. *Physical Review D*, 70(4):043008, 2004.

[32] M. Honda, T. Kajita, K. Kasahara, and S. Midorikawa. Improvement of low energy atmospheric neutrino flux calculation using the jam nuclear interaction model. *Physical Review D*, 83(12):123001, 2011.

[33] M. Honda, T. Kajita, K. Kasahara, S. Midorikawa, and T. Sanuki. Calculation of atmospheric neutrino flux using the interaction model calibrated with atmospheric muon data. *Physical Review D*, 75(4):043006, 2007.

[34] G. Hooft. Magnetic monopoles in unified gauge theories. *Nuclear Physics: B*, 79(2):276–284, 1974.

[35] N. Houston, T. Li, and C. Sun. A new solar neutrino channel for grand-unification monopole searches. *Journal of Cosmology and Astroparticle Physics*, 2018(10):034, 2018.

[36] T.-J. Irvine. *Development of neutron-tagging techniques and application to atmospheric neutrino oscillation analysis in Super-Kamiokande*. PhD thesis, University of Tokyo, 2014.

[37] C. Ishihara. *Full three flavor oscillation analysis of atmospheric neutrino data observed in Super-Kamiokande*. PhD thesis, Ph. D. thesis, Tokyo U, 2010.

[38] Y. Itow, T. Kajita, K. Kaneyuki, M. Shiozawa, Y. Totsuka, Y. Hayato, T. Ishida, T. Ishii, T. Kobayashi, T. Maruyama, et al. The jhf-kamioka neutrino project. *arXiv preprint hep-ex/0106019*, 2001.

[39] R. Jaffe and C. L. Smith. Deep-inelastic scattering, the subtraction of divergent sum rules, and chiral-symmetry breaking in the gluon model. *Physical Review D*, 7(8):2506, 1973.

[40] S. Kasuga, T. Hayakawa, S. Joukou, T. Kajita, Y. Koshio, T. Kumita, K. Matsumoto, M. Nakahata, A. Sakai, M. Shiozawa, et al. A study on the eμ identification capability of a water čerenkov detector and the atmospheric neutrino problem. *Physics Letters B*, 374(1-3):238–242, 1996.

[41] T. Kitagaki, H. Yuta, S. Tanaka, A. Yamaguchi, K. Abe, K. Hasegawa, K. Tamai, S. Kunori, Y. Otani, H. Hayano, et al. Charged-current exclusive pion production in neutrino-deuterium interactions. *Physical Review D*, 34(9):2554, 1986.

[42] H. Kume, S. Sawaki, M. Ito, K. Arisaka, T. Kajita, A. Nishimura, and A. Suzuki. 20 inch diameter photomultiplier. *Nuclear Instruments and Methods in Physics Research*, 205(3):443–449, 1983.

[43] V. Kuzmin and V. Rubakov. On the fate of superheavy magnetic monopoles in a neutron star. *Physics Letters B*, 125(5):372–376, 1983.

[44] K. Lodders. Solar elemental abundances. *arXiv preprint arXiv:1912.00844*, 2019.

[45] B. Louis, V. Sandberg, G. Garvey, H. White, G. Mills, and R. Tayloe. The evidence for oscillations. *Los Alamos Sci*, 25:16, 1997.

[46] G. Mitsuka. Neut. In *AIP Conference Proceedings*, volume 981, pages 262–264. American Institute of Physics, 2008.

[47] T. Mochizuki, J. Xia, M. Shiozawa, T. Yano, and Y. Nishimura. Development of a bleeder circuit of 50 cm diameter photomultiplier tubes for hyper-kamiokande. In *Proceedings of the 5th International Workshop on New Photon-Detectors (PD18)*, page 012001, 2019.

[48] M. Nakahata, K. Arisaka, T. Kajita, M. Koshiba, Y. Oyama, A. Suzuki, M. Takita, Y. Totsuka, T. Kifune, T. Suda, et al. Atmospheric neutrino background and pion nuclear effect for kamioka nucleon decay experiment. *Journal of the Physical Society of Japan*, 55(11):3786–3805, 1986.

[49] H. Nakamura and R. Seki. Quasi-elastic neutrino-nucleus scattering and spectral function. *Nuclear Physics B-Proceedings Supplements*, 112(1-3):197–202, 2002.

[50] J. Nieves, J. E. Amaro, and M. Valverde. Inclusive quasielastic charged-current neutrino-nucleus reactions. *Physical Review C*, 70(5):055503, 2004.

[51] H. Nishino, K. Awai, Y. Hayato, S. Nakayama, K. Okumura, M. Shiozawa, A. Takeda, K. Ishikawa, A. Minegishi, and Y. Arai. High-speed charge-to-time converter asic for the super-kamiokande detector. *Nuclear Instruments and Methods in Physics Research Section A: Accelerators, Spectrometers, Detectors and Associated Equipment*, 610(3):710–717, 2009.

[52] S. Orito, H. Ichinose, S. Nakamura, K. Kuwahara, T. Doke, K. Ogura, H. Tawara, M. Imori, K. Yamamoto, H. Yamakawa, et al. Search for supermassive relics with a 2000-m 2 array of plastic track detectors. *Physical review letters*, 66(15):1951, 1991.

[53] L. K. Pik. Study of the neutrino mass hierarchy with the atmospheric neutrino data observed in super-kamiokande. *n. o October*, 2012.

[54] H.-K. Proto-Collaboration, K. Abe, et al. Hyper-kamiokande design report. *KEK-Preprint-2016-21, ICRR-Report-701-2016-1, https://lib-extopc. kek. jp/preprints/PDF/2016/1627/1627021. pdf*, 2016.

[55] A. Rajantie. Magnetic monopoles in field theory and cosmology. *Philosophical Transactions of the Royal Society A: Mathematical, Physical and Engineering Sciences*, 370(1981):5705–5717, 2012.

[56] D. Rein. Angular distribution in neutrino-induced single pion production processes. *Zeitschrift für Physik C Particles and Fields*, 35(1):43–64, 1987.

[57] D. Rein and L. M. Sehgal. Neutrino-excitation of baryon resonances and single pion production. *Annals of Physics*, 133(1):79–153, 1981.

[58] A. Renshaw, K. Abe, Y. Hayato, K. Iyogi, J. Kameda, Y. Kishimoto, M. Miura, S. Moriyama, M. Nakahata, Y. Nakano, et al. First indication of terrestrial matter effects on solar neutrino oscillation. *Physical review letters*, 112(9):091805, 2014.

[59] S. Roesler, R. Engel, and J. Ranft. Photoproduction off nuclei: Particle and jet production. *Physical Review D*, 57(5):2889, 1998.

[60] V. Rubakov. Pis' ma zh. eksp. theor. fiz. 33 (1981) 658 [jetp lett. 33 (1981) 644]. *Nucl. Phys. B*, 203:311, 1982.

[61] K. Sato. Cosmological baryon-number domain structure and the first order phase transition of a vacuum. *Physics Letters B*, 99(1):66–70, 1981.

[62] M. Shiozawa. Reconstruction algorithms in the super-kamiokande large water cherenkov detector. *Nuclear Instruments and Methods in Physics Research Section A: Accelerators, Spectrometers, Detectors and Associated Equipment*, 433(1-2):240–246, 1999.

[63] S. Singh, M. Vicente-Vacas, and E. Oset. Nuclear effects in neutrino production of δ at intermediate energies. *Physics Letters B*, 416(1-2):23–28, 1998.

[64] T. Sjostrand. Pythia 5.7 and jetset 7.4 physics and manual. *arXiv preprint hep-ph/9508391*, 1995.

[65] R. Smith and E. J. Moniz. Neutrino reactions on nuclear targets. *Nuclear Physics B*, 43:605–622, 1972.

[66] A. Suzuki, M. Mori, K. Kaneyuki, T. Tanimori, J. Takeuchi, H. Kyushima, and Y. Ohashi. Improvement of 20 in. diameter photomultiplier tubes. *Nuclear Instruments and Methods in Physics Research Section A: Accelerators, Spectrometers, Detectors and Associated Equipment*, 329(1-2):299–313, 1993.

[67] I. U. Tokyo. Super kamiokande home page. *http://www- sk.icrr.u-tokyo.ac.jp/sk/*, 2019.

[68] K. Ueno, K. Abe, Y. Hayato, T. Iida, K. Iyogi, J. Kameda, Y. Koshio, Y. Kozuma, M. Miura, S. Moriyama, et al. Search for gut monopoles at super–kamiokande. *Astroparticle Physics*, 36(1):131–136, 2012.

[69] T. F. Walsh, P. Weisz, and T. T. Wu. Monopole catalysis of proton decay. *Nuclear Physics B*, 232(2):349–355, 1984.

[70] R. Wendell, C. Ishihara, K. Abe, Y. Hayato, T. Iida, M. Ikeda, K. Iyogi, J. Kameda, K. Kobayashi, Y. Koshio, et al. Atmospheric neutrino oscillation analysis with subleading effects in super-kamiokande i, ii, and iii. *Physical Review D*, 81(9):092004, 2010.

[71] J. Wentz, I. M. Brancus, A. Bercuci, D. Heck, J. Oehlschläger, H. Rebel, and B. Vulpescu. Simulation of atmospheric muon and neutrino fluxes with corsika. *Physical Review D*, 67(7):073020, 2003.

[72] Wikipedia contributors. Photomultiplier tube — Wikipedia, the free encyclopedia, 2021. [Online; accessed 13-July-2021].

[73] R. J. Wilkes. Results on neutrino oscillations from super-kamiokande. *Advances in Space Research*, 26(11):1813–1822, 2000.

[74] T. Yokozawa. *Precision solar neutrino measurements with Super-Kamiokande-IV*. PhD thesis, PhD thesis, U. Tokyo (main), 2012. http://www-sk. icrr. u-tokyo. ac. jp/sk . . . , 2012.

Appendix A

MCP PMT Flasher Measurement

A.1 Hyper-Kamiokande Experiment

The Hyper-Kamiokande detector is a large water Cherenkov detector scheduled to be built at 8 km south of Mt. Ikeno, where the Super-Kamiokande detector is located, 650 m underground of Mt. Ninjugo. It contains 190,000 tons of water, which is 8.4 times as much as the SK water tank. The tank is divided into two layers, an inner tank and an outer tank with a coaxial center. The inner tank is mainly equipped with about 40,000 20-inch diameters PMTs inward for neutrino observation, and the outer tank is mainly installed 8 inch PMT to eliminate cosmic ray-derived events. The photoelectric surface coverage of PMT is about 40% in the inner water tank.

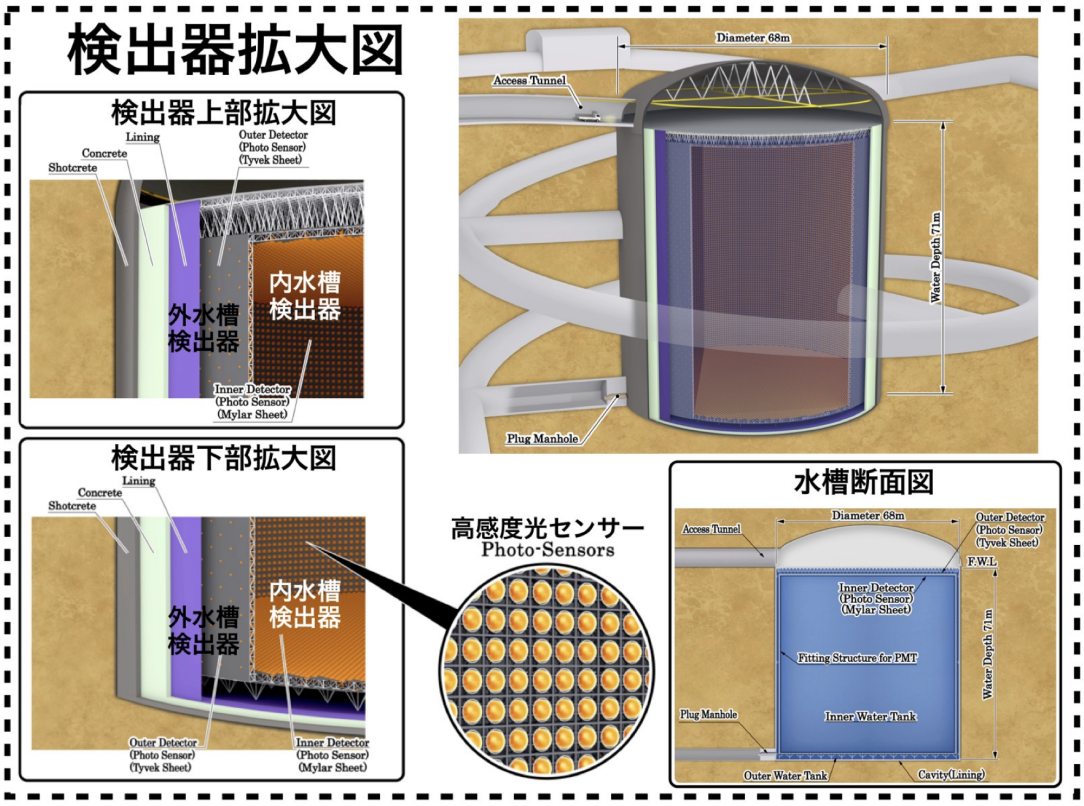

Figure A.1: Hyper-Kamiokande detector

The tank is cylindrical with a diameter of 68.0 m and a height of 71.0 m. The inner water tank has a diameter of 64.8 m and a height of 64.8 m, and the area of 2m above and below the outside and 1 m outside the side surface is the outer water tank. In the Super-Kamiokande detector, the tank was made of stainless steel to prevent the contamination of radioactive substances such as radon from the bedrock, in the same way as the Super-Kamiokande detector. However, the material of the tank itself and the material between the tank and the bedrock is currently being studied.

The inner and outer tanks are separated by a stainless steel structure for arranging the PMT. The excavation cavity has the shape of a cylinder in which the tank is placed and a dome above it. The top and side surfaces of the structure in which this PMT is placed are suspended from the ceiling of this dome-shaped space. This has been changed from the

method adopted in the Super-Kamiokande detector in consideration of making the structure thinner and lighter.

In addition, since the geomagnetism in the vertical direction will affect the photon collection efficiency of the PMT, rectangular and circular coils are arranged in the vertical and horizontal directions of the tank to cancel the geomagnetism. If necessary, further consideration will be given to the installation of coils.

A.2 The MCP PMT

One of the important elements in the water Cherenkov detector is the photodetector. Hyper-K plans to use about 40,000 photodetectors in the inner water tank and about 8,000 photodetectors in the outer water tank. The particle type, energy, reaction position, etc. are reconstructed by using the charge and time information obtained by these photodetectors. Photodetectors are subject to various requirements because these reconstructions require information in units of one photon and several ns, respectively. Table 3.1 summarizes the performance requirements for photodetectors in Hyper-K.

	Item		Condition	Remark
Single P.E.	Peak to Valley ratio	> 1.9	Typical	
	Charge resolution	< 50 %	σ, Typical	
	Time resolution	< 1.2 ns	σ, Typical	
Response	Rise time	< 10 ns	10%-90%H, Typical	
	Pulse width	< 200 ns	Typical, 95% area	Fast recovery of baseline level
Gain	Detection efficiency	> 0.29	Typical, at 0.25 P.E.	QE 30% x CE 95% assumed
	Gain	1E7	Typical	
	Gain transition (Aging)	> -10 %	In 10 years	At same bias voltage
	Stabilization	< 1%	In 1 hour	Referring to stable level
	Gain variation in magnetic field	< 10%	200 mG	For both gain and efficiency
	Dynamic range	1-1000 P.E.	At 1E7 gain	< 10% linear response by 500 P.E.
	Rate tolerance	< 10%	0.1 A	= 50 PE x 1 MHz for example
Noise	Dark count rate	< 4 kHz	Typical, at 0.25 P.E.	At 15 ℃
	Flasher rate	0 Hz MAX	> 100 P.E. thres.	
	Flasher failure rate	< 0.01 %	In 10 years	In water tank
	After pulse rate	< 5%	In 10 μs, > 0.25 P.E.	Relative to primary 1 PE pulses
Long Operation	Lifetime	> 20 years		In design
	Failure rate	< 1%/year	In 10 years	Exclude initial 1 year operation
	Initial failure rate	< 5%/year	In 1 year	After operation starts, Guaranteed
	Length	< 70 cm		
	High pressure tolerance	> 1.2 MPa	Min, In water	All PMTs will be tested
	Deadline for delivery	2024 mid		Assuming construction from 2018
	Ordering quantity	40k	Max	

Figure A.2: performance requirements for photodetectors in Hyper-K

NNVT has been producing 20-inch PMTs based on micro-channel plates (MCP), which is already applied to the JUNO experiment. Those PMTs had a good detection efficiency (30%), good pressure tolerance, and low radio-isotope glass. However, their weak point was their timing resolution of approximatively 20 ns, which was insufficient for use in Hyper-Kamiokande. NNVT developed a new version with focusing electrodes to improve the timing resolution. Coupled with an optimization of the voltage divider circuit, they allowed this new model to reach a timing resolution of 4.3 ns (FWHM), better than the resolution of the HPK R3600 used in Super-K (6.73 ns). This improved MCP PMT, the GDB-6203, is now tested as an alternative option for the Hyper-Kamiokande inner detector.

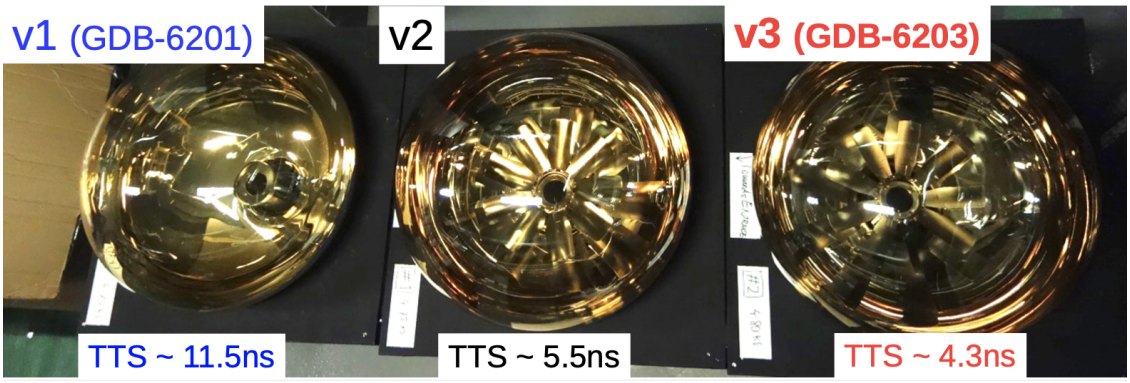

Figure A.3: The MCP PMT

A.3 The MCP PMT Flasher Measurement

From the above table, we can see whether a flasher has existed as an important feature for us to detect the photomultiplier tube (PMT). If there are flashers, especially flasher amplitude is greater than 100 pe, the systematic error will be increased. As we described in Chapter 5 and Chapter 6.

The main reason for the flasher is caused by the PMT dynode discharge. So when we measure the flasher. We need to put PMT in an experiment box that is completely shaded

and has no background as much as possible and use two PMT that have been confirmed to have no flasher, as monitoring PMT. The schematic diagram and photos of the experimental equipment are shown in the figure below. If there is a signal greater than 100 pe, we will observe the three PMT simultaneously appear flasher coincident signals.

We use two methods when measuring the flash characteristics of MCP PMT. The first method is an indirect measurement, that is we do not directly observe the monitor PMT signal to determine whether this signal is a flash signal or not. We measure the monitor PMT event rate which is more than 100 p.e. If MCP PMT does not produce a flash signal, then the 100 p.e signal rate of the monitored PMT under long-term observation should be at the same level as the background 100 p.e signal rate, which is the 100 p.e signal rate when the MCP PMT is turned off.

However, if MCP PMT will continuously emits flash signals, the 100 p.e signal rate of monitoring PMT should be quite different from the background 100 p.e signal event rate. A very important advantage of this method is that we can measure MCP PMT for a long time. But there is still a disadvantage that is that we cannot determine whether the 100 p.e signal comes from MCP PMT or not, since we couldn't make a pure environment which is no 100 p.e emit source.

We already know that the flashing characteristics of MCP PMT are positively correlated with the working voltage of PMT, so when we perform an indirect measurement, we will start measuring from 0 and rise the voltage step by step. Each step is measured for 20 minutes to calculate an average signal rate. At the same time, we also set up a coincidence signal here. If there is a flash event, then the two PMT will have a coincidence signal.

But when we performed the first measurement, we found that whether it was a 1-inch monitoring PMT or a 20-inch monitoring PMT, their 100 p.e signal rate did not increase significantly compared to when the MCP PMT was turned off. Therefore, we gave up the

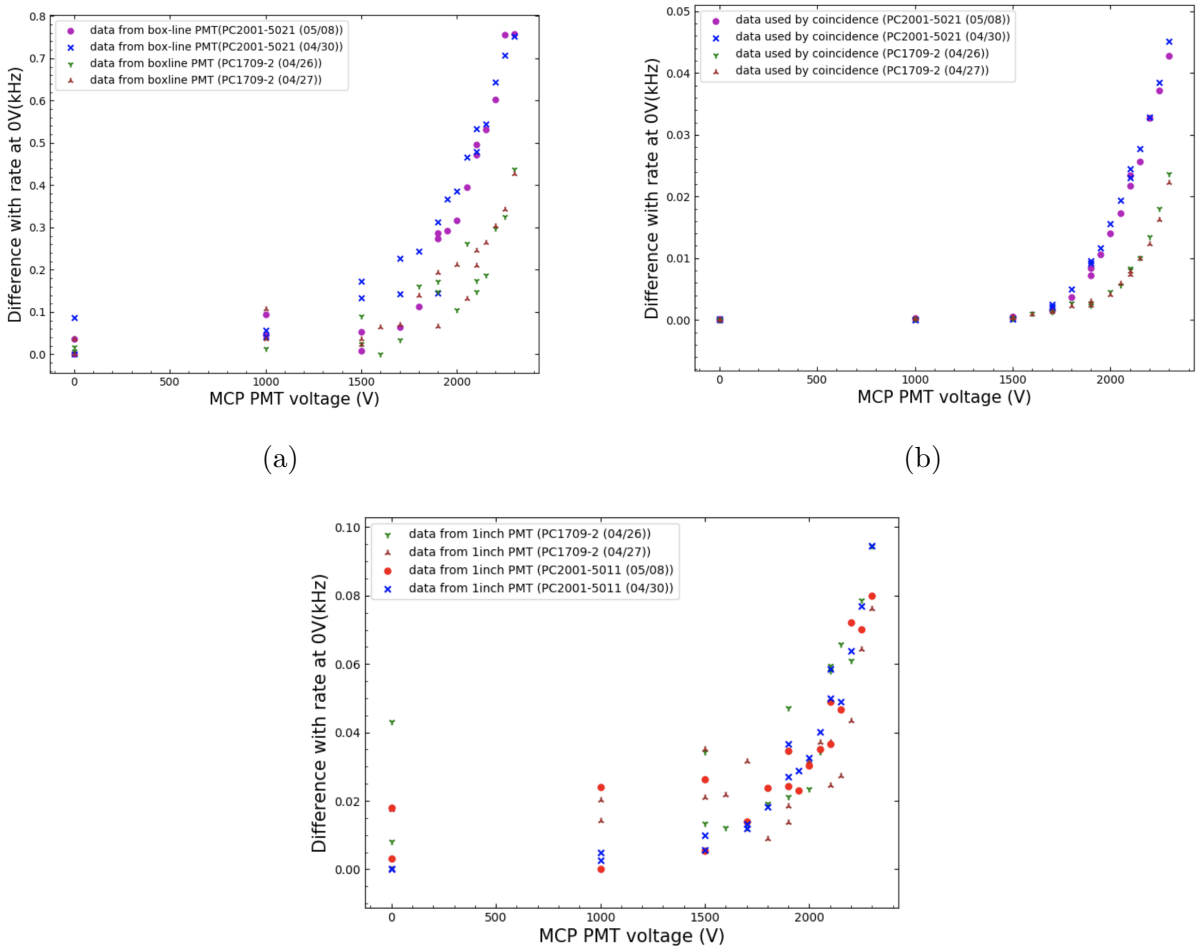

Figure A.4: The result of indirect measurement of the flash characteristics of MCP PMT. The three pictures are one-inch PMT 100 p.e signal event rate (c), 20-inch SK PMT 100 p.e signal event rate (monitoring PMT) (b), and the coincidence signal 100 p.e signal event rate (the coincidence signal is 20-inch PMT and the coincidence with the signal of 1 inch PMT) (a). The dot and the triangle point represent the 100 p.e signal measurement result when the MCP PMT is working. The inverted triangle point and the cross represent the measurement result when closed MCP PMT (background).

indirect method, and check the MCP PMT will emit a flash signal or not by using the direct method, that is an oscilloscope is directly used to observe the MCP signal to determine whether a flash signal appears.

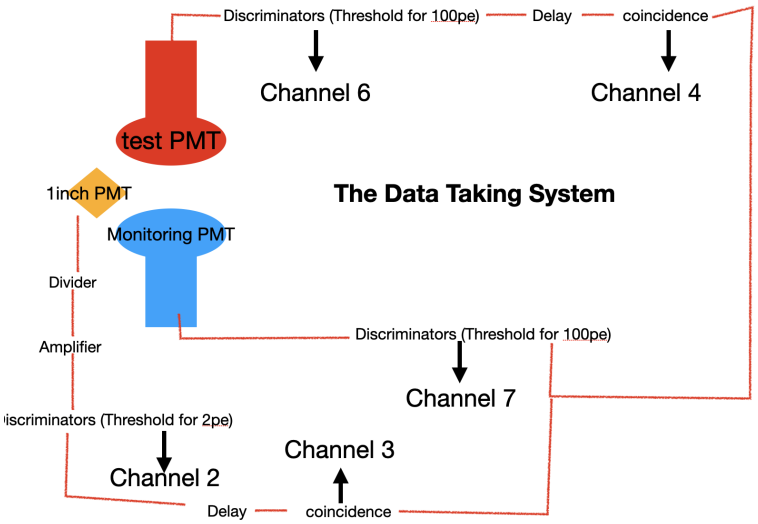

Figure A.5: Schematic diagram of flasher measurement of MCP PMT

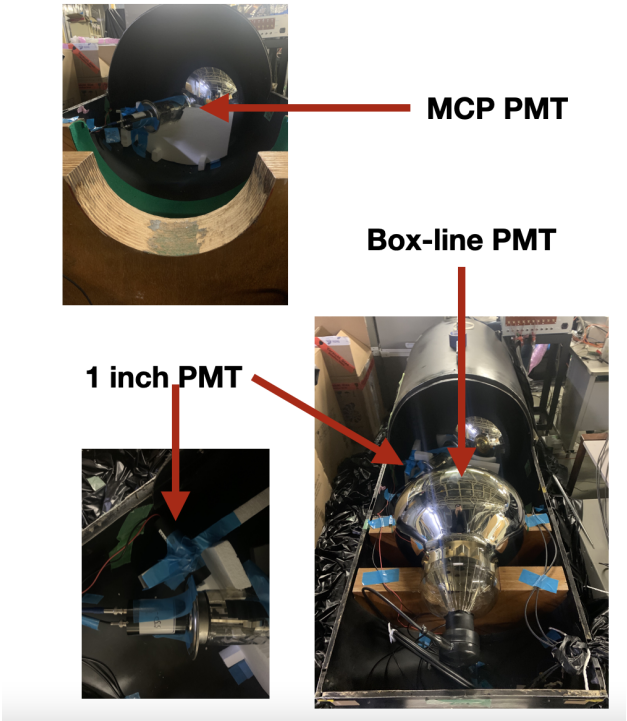

Figure A.6: Photos of flasher measurement of MCP PMT

After about 30 days of long-term observation, we have confirmed that MCP PMT will show about three flashes per hour. This does not meet the requirements of HK for photo-multiplier tubes. Therefore, we need to invite NNVT to further conduct MCP PMT. The improvement, because MCP PMT has very good cost performance and detection efficiency.

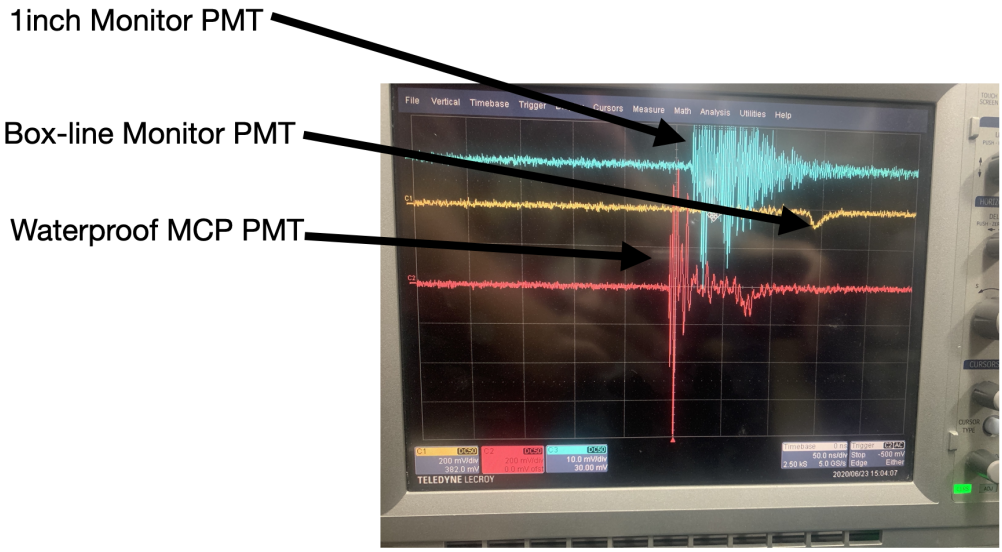

Figure A.7: A example of MCP PMT flasher event